uc3m | Universidad Carlos III de Madrid

NUMERICAL AND EXPERIMENTAL ANALYSES OF A SOLID IMPACTING A WATER SURFACE

Bachelor's thesis

Bachelor's degree in Aerospace Engineering

Academic Year (2018-2019)

Author:

Gregory Anthony Turri

Tutor:

Javier Rodríguez Rodríguez

June 2019, Leganés, Spain.

ABSTRACT

To date, water-impact events remain an unsolved problem from both a mathematical and a numerical point of view. Complex hydrodynamic phenomena are involved in the study of this problem. Several authors have attempted to describe these phenomena analytically and numerically, but a general model remains yet unclear. Nowadays, efforts are concentrated on the fluid-structure interaction (FSI), as this influences the results dramatically. Recent advances on FSI indicate that several challenges arise from high-fidelity fully-coupled water-impact problems, where both global and local phenomena cannot be reproduced accurately at the same time. This projects proposes a simple yet promising approach to model the fluid domain within the fluid-structure interaction of the problem. The dimensionless Navier-Stokes equations for the case of an incompressible variable-density flow are solved by means of the open-source software *Basilisk*. Numerical simulations are compared with experiments, yielding noteworthy results. The main characteristics of the flow gathered in experimental observations were reproduced numerically, with a higher degree of accuracy in some cases than in others. Still, improvements must be made before adopting this methodology for vertical impacts or ditching events. Particularly, the approach used to impose the boundary condition on the solid must be revised and possibly discarded. If that were the case, the embedded boundaries technique would be a strong candidate. Furthermore, additional sources in the convergence of results, such as surface tension or bubbles-droplets removal, could be subjected to analysis.

Contents

List of Figures

List of Tables

Acronyms

ALE Arbitrary Lagrangian-Eulerian

AMC Acceptable Means of Compliance

AMR Adaptive Mesh Refinement

BC Boundary Condition

CFD Computational Fluid Dynamics

CFL Courant–Friedrichs–Lewy number

EASA European Aviation Safety Agency

FE Finite Element

FSI Fluid-Structure Interaction

NACA National Advisory Committee for Aeronautics

PDE Partial Differential Equation

RANS Reynolds-averaged Navier–Stokes

SPH Smooth-Particle Hydrodynamics

VOF Volume of Fluid

1 General Introduction

1.1 Motivation and context

The idea for this Bachelor's thesis came from the possibility of implementing the use of the CFD software *Basilisk* [1] in problems regarding the impact of solids into water surfaces. Such problems are fairly complex due to the strong interaction between the solid's structure and the fluid. The wide range of spatial scales often encountered in this type of fluid flows make adaptive mesh refinement algorithms, like *Basilisk*, particularly noteworthy. This will be further developed in section 4.1.

Delivering accurate and cost-effective solutions to technological challenges is one of the main roles of an engineer. In addition, the opportunity of expanding the possibilities of an open-source software, as the one used in this project, made this challenge undoubtedly appealing. Moreover, the experience gained throughout the whole process was motivated by the ability to generate an initial know-how of this software for the Fluid Mechanics Research Group at UC3M, whose members are already familiarized with *Basilisk*'s predecessor, *Gerris* [2].

When it comes to structural bodies impacting surfaces of water, several applications can be thought of for the aerospace industry, for instance, ditching events, seaplanes and flying boats landing, or spacecraft splashdown, to name a few.

Figure 1.1: Ditching event [3]

Figure 1.2: Seaplane landing [4]

Figure 1.3: Flying boat landing [5]

Figure 1.4: Apollo 9 Splashdown [6]

Considerable research has been carried out to shift the efforts from costly and lengthy testing campaigns of real models, sometimes only certain parts of the structure or even scale models due to budget constraints, to reliable and realistic numerical models, as it is presented in section 1.2.

1.2 State of the art

Several authors, such as Theodore von Kármán [9], Herbert A. Wagner [12] and Alexander A. Korobkin [17, 19, 21, 24], have tried to develop analytical theories for water-impact problems. In the last decades, efforts have focused on developing numerical models that can cope with the overall complexity of the problem.

One of the first significant contributions was proposed by Theodore von Kármán in 1929 [9]. He sought to develop a theoretical formula to calculate the maximum pressure on floats of landing seaplanes. The model started from a wedge-shaped geometry and took into account the increased inertia due to the added mass of the fluid. Based on the momentum theorem, he was able to determine the force developed on the impacting body. Von Kármán found that the maximum pressure occurs at the middle of the float exactly at the instant of impact, which decreases as the deadrise angle increases, i.e., sharper bodies. These results were consistent with experiments he referenced to make the comparison, which were developed some years before [7, 8].

Between the 1930s and 1950s the theoretical and experimental foundations on water impact problems were laid down. Experimental research was carried out during these years mainly by NACA and the U.S. Navy Office of Naval Research. The first publication concerning regular aircrafts was published in 1953, presenting experimental data on rear-fuselage shapes under ditching [15]. However, these experiments were influenced by inaccuracies associated with the scaling of hydrodynamics phenomena.

In 1945, NACA's reports [10, 11] provided the groundwork for the first publications of fluid-structure interaction on flying-boats. Fundamentally, they considered the hydrodynamic force component coming from the planing action (horizontal velocity), which had not been done until then. Moreover, a thorough review of the literature up to 1945 was presented in [11]. In this report, the author investigated the correlation of previous theories with contemporary experiments for oblique impact, demonstrating how they overestimated the impact forces. His proposed theory showed satisfactory correlations with experimental data for vertical drop, oblique impact and planing.

Later on, the theory and experiments developed for the FSI dilemma were presented in [13, 14]. However, they did not regard the change in pitching moment in the equations of motion, based on the presumption that although it could be large, the impact characteristic *time* was still short enough to neglect developed angular velocities and displacements. Remarkable conclusions were reached in terms of the hydrodynamic force and accelerations. Indeed, it was shown how the structural response may have a substantial effect on the hydrodynamic force, being able to modify its time history shape and the maximum value. Additionally, the theoretical time histories of the accelerations of the center of gravity and the associated with elastic structural response presented satisfactory agreement with the experiments.

Efforts started to evolve towards numerical simulation techniques in the 1980s. One of the first methods to gain attention was SPH (Smooth-particle hydrodynamics). Originally developed for astrophysical problems, it was later used in combination with FE methods to investigate impact problems in both the aeronautical and naval fields. H. Climent *et al.* [18] showed the accuracy of this methodology when considering vertical impacts only. However, when analyzing aircraft ditching with a horizontal velocity component, results in both the calculated pressures on the structure as well as in its kinematic evolution were significantly different from those obtained in the scale model experiment. These unsuccessful outcomes came from the nature of the SPH formulation, which makes the methodology unstable in negative pressure regions, an incident known as *tensile instability*. Therefore, the rear part of the fuselage did not experience neither the proper suction forces nor cavitation and ventilation phenomena.

The particular methodology followed in [18] was basically a hybrid SPH-Lagrangian approach to improve the accuracy of a pure SPH method. SPH particles were placed in the fluid regions where deformations were expected to be large, and Lagrangian elements elsewhere. The interactions between the SPH particles and the Lagrangian mesh were enforced through a penalty contact algorithm. However, two difficulties arose from this approach. First, the definition of proper contact parameters at the interface between the FEs and the SPH particles. Second, the choice of amount of fluid volume to be replaced by the Lagrangian mesh without affecting the accuracy of the results.

During the last decades, several techniques have been investigated in order to identify the most suitable one for simulating ditching problems. C. Bisagni and M. S. Pigazzini [27] used the commercial software *LS-DYNA* to compare two fluid simulation techniques with experimental data from the literature for a rigid airplane ditching. First, the ALE (Arbitrary Lagrangian–Eulerian) approach was used. This methodology consists on calculating several Lagrangian steps followed by an advection one where material is transported through the elements and the computational grid is either translated in space or reshaped into its original configuration. The second approach, hybrid Lagrangian-SPH, was the same as the one used in [18].

C. Bisagni and M. S. Pigazzini [27] concluded that the hybrid Lagrangian-SPH approach did not properly account for suction forces, which was the same conclusion reached in [18]. In addition, although the ALE approach showed good correlation with experiments, it overestimated the value of the suction force and predicted that both longitudinal and vertical accelerations were of the same magnitude. As pointed out by the authors, this last findings seemed a very unlikely loading condition for an airplane. Nonetheless, both approaches agreed that maximum deceleration does not occur at the impact time but after, due to the generation of hydrodynamic phenomena.

Other authors have investigated different effects on airplane ditching, such as that of the pitch angle [22]. Using a RANS solver for an unsteady compressible flow together with $k-\epsilon$ to model turbulence, and a VOF method to track the interface, the authors concluded that, for a rigid airplane, a pitch angle between 10°-12° was recommended as the aircraft would pitch down gradually in a tender motion.

Flexibility is another determinant factor on the accuracy of the results. In [29], P. Vega-Martínez, J. Rodríguez-Rodríguez, A. A. Korobkin *et al.* demonstrated experimentally the importance of flexibility considerations to compute fluid-structure interaction. Although the experiment treated a water-exit problem at large acceleration, it is still noteworthy to extrapolate concepts for ditching problems, mainly the suction phenomena.

The authors of [29] introduced hydroelastic effects to the theory proposed by A. A. Korobkin [23]. In the latter, the author developed a linearized analytical theory to match the numerical results presented by D. J. Piro and K. J. Maki [20]. In such theory, hydrodynamic equations and boundary conditions were linearized exploiting the fact that at small times, displacements are small. The hydrodynamic pressure was found to be negative in magnitude (suction) and maximum at the center of the wetted area, being the latter a key parameter for the generation of the hydrodynamic force. The maximum value of this negative force occurred at the instant where the velocity of the body was zero, as found in the numerical results of [20].

Coming back to [29], the authors showed how the acceleration changed dramatically when compared to the theoretical one, once a certain critical time ($t_{critical} \approx 4.5ms$) was reached. As proved by the authors, this had to do with the assumption of rigid plate in the original theory of [23]. They were able to correlate the modified analytical results with the experimental ones, proving how the acceleration at the center of the disc did not monotonically increase even if the force did, and the wetted surface did not shrink immediately. These findings came from the introduction of elastic effects in this modified theory, and considering only the first normal mode of the disc.

Although the original linear theory proposed in [23] works fine for very short times, the complexity of the problem, for times above the critical one, was satisfactorily overcome by introducing linear elastic effects. This certainly shows the importance of the elastic behaviour of structures in ditching and other water-impact/exit problems.

With regard to flexibility in ditching problems, other authors have proposed different approaches. H. Climent, G. Pastor and J. T. Viana [26] used pressure readings from previous tests and introduced a correction strategy in the FE model based on the deformation of the local height and pitch angle. Accurate deformation shapes in time history were obtained, as well as accurate time of occurrence of peak deformation. However, the deformation levels were not conservative, overestimating the alleviating effects of flexibility.

As previously suggested, most current research is concentrated on the fluid-structure coupling field. As demonstrated by M. Müller, M. Woidt, M. Haupt *et al.* [28], several challenges arise when examining highly coupled structural bodies impacting water surfaces, as three elements must be properly characterized. First, the structural simulation presents regions on concentrated damage, thus generating large differences in the scales of the model. Similarly, the fluid simulation not only involves multiphase phenomena, but also intricate hydrodynamic phenomena such as cavitation and suction. Finally, if standard Dirichlet-Neumann boundary conditions are adopted, then, using an explicit structural solver with an explicit coupling procedure yields an unstable method due to the significant added-mass effect. In such case, both an implicit structural solver and coupling procedure should be used.

Taking this into account, M. Müller, M. Woidt, M. Haupt *et al.* proposed a method that combined a multiphase flow solver (*interDyMFoam, OpenFOAM*), the implicit *Abaqus* solver, and an implicit coupling procedure. The last one enforces several iterations until a convergence criterion on the displacement is reached. The authors demonstrated the validity of the procedure for both rigid and deformable structures, in addition to showing the impracticability of simulating both the structural damage and the overall dynamics of the aircraft.

Aircraft manufacturers are currently investing considerable efforts to obtain reliable numerical tools that can replace expensive and lengthy experimental campaigns. Finding rigorous and efficient CFD tools capable of reproducing all the hydrodynamic phenomena involved in the problem discussed, as well as establishing procedures to accurately reproduce the fluid-structure interaction, are the main difficulties to be solved.

1.3 Objectives

The main objective was to generate an initial know-how about the *Basilisk* software. With this, the Fluid Mechanics Research Group at UC3M will be able to gradually replace *Gerris* for *Basilisk*.

Moreover, this project aimed to determine the feasibility of generating a simple yet valid CFD model to be used in fluid-structure interaction problems.

1.4 Document outline

This Bachelor's thesis is organized as follows:

Section 2 presents an introduction to the phenomena involved in water impact problems and discretizes the overall domain from a mathematical point of view. Here, the proposed equations of motion governing the flow are presented.

Section 3 covers the experimental procedure followed. The designed structure, experiments performed and data gathering are explained in this section.

Section 4 covers the fundamental features of the program used and presents the numerical code implemented to simulate the experimental cases. Here, the numerical schemes supporting the code are briefly explained. Finally, the effect of the level of mesh refinement on the results is inspected.

Section 5 discusses the results obtained from experiments and simulations, in addition to comparing the evolution of the interfaces.

Section 6 discusses some noticeable outcomes. Furthermore, several suggestions are proposed to continue and improve the methodology.

Section 7 presents the budget analysis for the project and develops an analysis on the socio-economical implications.

Section 8 covers the regulatory framework concerning the certification requirements for ditching events.

2 Introduction to the problem

Structural bodies impacting into water surfaces present a complex problem, mainly integrating aerodynamics, hydrodynamics, and structural dynamics.

Although different applications can be found for this problem (see section 1.1), all might be characterized by four phases: *approach, impact, landing,* and *floatation*. The *landing* phase corresponds to the interval between the *impact* phase and complete stoppage. The *floatation* phase corresponds to the instants following the complete stoppage. In this project, the efforts were focused mainly on the *impact* phase of a **vertical** water-collision.

Initially, the body moves downwards (in a vertical motion) displacing the air surrounding it, thus generating an aerodynamic force. As soon as the body impacts the water, the "instantaneous" (occurring in a very short time) increase of pressure in the fluid is transmitted at the speed of sound (of water). Therefore, the waves generated from this initial times can be neglected in a first approach due to their short wavelength and low energy.

Entry loads are characterized by the dynamic pressure, which means that they are proportional to the entry velocity squared. On the other hand, water-exit problems are governed by the acceleration, provided that it is much larger than the gravitational one. If the acceleration of the body is smaller than the gravitational acceleration, then gravity and the hydrostatic pressure characterize the physics of the problem, as proved in [29].

Several hydrodynamic effects take place simultaneously in impact problems, such as:

- Suction
- Cavitation
- Ventilation
- Air-cushioning
- Spray
- Water elasticity (Surface tension)

Each of these plays an important role when analyzing certain variants of the impact problem. Suction is one of the most dominant hydrodynamic effects in problems with a horizontal velocity (ditching events, seaplanes landing). Unlike vertical impact problems, the horizontal velocity introduces another component on the flow and, thus, increases its complexity. As seen in section 1.2, reproducing suction for the correct simulation of the problem is crucial, as it is the main source of the deceleration of the aircraft once it has impacted. Cavitation appears when sudden changes in the pressure of the fluid lead to the immediate generation of cavities of fluid vapour with a relative pressure lower than the fluid surrounding it.

This might lead to shock waves and all the effects associated with them, which may damage structural bodies nearby.

2.1 Mathematical description of the problem

As previously mentioned, efforts were focused on vertical water impact problems. After inspecting the nature of the problem, it was decided that the part corresponding to the fluid domain could be well represented by solving the Navier-Stokes equations for the case of an incompressible variable-density flow.

As it is presented in section 3, given an approximate impact velocity $U = 1.07[m/s]$ (for the fastest experimental case developed), the radius of the cylinder section used in the experiment $R = 90.83\ [mm]$, and the properties of water at the temperature of the day of the experiments ($T = 25°C$), the Reynolds number can be computed as

$$Re = \frac{\rho U R}{\mu} = 109073.66 \tag{2.1}$$

Equation 2.1 indicates that convective terms are of a much higher order than viscous ones. Nonetheless, viscosity was still considered in order provide a means of flow energy dissipation and, thus, mitigate unrealistic non-linear instabilities that could arise.

Gravity was also required in order to accurately represent the physics of the flow, as it can be quickly checked computing the Froude number:

$$Fr = \frac{U}{\sqrt{(gR)}} = 1.13 \tag{2.2}$$

This indicates that the order of magnitude of gravity forces is at least of the same order of magnitude as inertial forces.

Inspecting both dimensionless numbers for real case scenarios of water impact (ditching, seaplane landing), where sink speeds are not below 1.5 [m/s], yield larger values of both the Reynolds and the Froude number. In such scenarios, inertial forces play even a more crucial role than viscous or gravitational ones. Still, the experiments developed served as a first approach towards the tackling of these kind of problems, as it will be discussed in section 5.

Then, Navier-Stokes equations were non-dimensionalized not only to identify the relevancy of each term on the problem, but also to generate a non-dimensional code able to simulate different cases just changing two parameters, i.e., Reynolds and Froude number. The mass continuity and momentum equations, 2.3 and 2.4 respectively, are presented in differential form.

$$\frac{\partial \rho}{\partial t} + \nabla \cdot (\rho \mathbf{u}) = 0 \tag{2.3}$$

$$\rho \frac{D\mathbf{u}}{Dt} = -\nabla p + \nabla \cdot \boldsymbol{\tau} + \rho \mathbf{g} \tag{2.4}$$

Considering an incompressible flow and developing the material derivative and the viscous stress tensor, the equations above become:

$$\nabla \cdot \mathbf{u} = 0 \tag{2.5}$$

$$\rho \frac{\partial \mathbf{u}}{\partial t} + \rho \mathbf{u} \cdot \nabla \mathbf{u} = -\nabla p + \mu \nabla^2 \mathbf{u} + \rho \mathbf{g} \tag{2.6}$$

Then, selecting as characteristic variables of the problem the radius of the cylinder R and the impact velocity U, the dimensionless variables and operators of the problem can be obtained as:

$$\mathbf{u}^* = \frac{\mathbf{u}}{\sqrt{gR}} \; ; \; p^* = \frac{p}{\Delta p} \; ; \; \mathbf{x}^* = \frac{\mathbf{x}}{R} \; ; \; t^* = \frac{tU}{R} \; ; \; \nabla^* = R\nabla \tag{2.7}$$

Substituting the terms of 2.7 in the momentum equation 2.6 the following expression is obtained:

$$\frac{\partial \mathbf{u}^*}{\partial t^*} + \mathbf{u}^* \cdot \nabla^* \mathbf{u}^* = -\nabla^* p^* + \frac{1}{Re} \nabla^{*2} \mathbf{u}^* - \frac{1}{Fr^2} \mathbf{g} \tag{2.8}$$

Therefore, taking advantage of this compact form, all the experimental cases were simulated mainly changing the Reynolds and the Froude numbers, as it can be seen in section 4.2.1.

Finally, the boundary conditions of the problem were selected considering the nature of the flow. The left, bottom and right boundaries of the domain were characterized as solid walls with no penetration conditions, eq. (2.9). The upper boundary was treated as an outflow boundary, eq. (2.10). Finally, the solid imposes a no penetration condition eq. (2.11), where the velocity of the flow must be the same as the one of the solid in the normal direction.

$$u_n\Big|_{left} = u_n\Big|_{bottom} = u_n\Big|_{right} = 0 \tag{2.9}$$

$$p\Big|_{top} = 0 \; and \; \frac{\partial \mathbf{u}}{\partial n}\Big|_{top} = 0 \tag{2.10}$$

$$u_n\Big|_{solid} = v_{solid,n} \tag{2.11}$$

The sub index n stands for the local normal coordinate of a vector with respect to a boundary.

3 Experimental procedure

In this section, the experimental process followed to analyze the impact of a solid is presented. The aim of the experiments was to validate the usage of the programmed code for the applications mentioned in section 1.1.

3.1 Experimental setup

Experiments were carried out in the wave flume located in the Fluid Mechanics Department facilities, at UC3M (see fig. 3.1). The test section has a cross section of 25x25 $[cm^2]$ and the top portion is open, exposed to atmospheric air. Two laterals glass plates and a bottom methacrylate one conform the walls of the test section.

Figure 3.1: Closed-loop wave channel

The experimental setup (see fig. 3.2) consisted of a structure mounted on a portion of the flume's test section. It was originally designed using the software *Solid Edge* and manufactured with several materials. The cylinder portion is a solid piece of Polyvinyl chloride (PVC), as well as the lower and upper plates and the central capsule. Stainless steel shafts and sintered bronze bushings coordinate the vertical movement of the structure. The weight of the test structure (excluding the upper plate) is 1.637 kg.

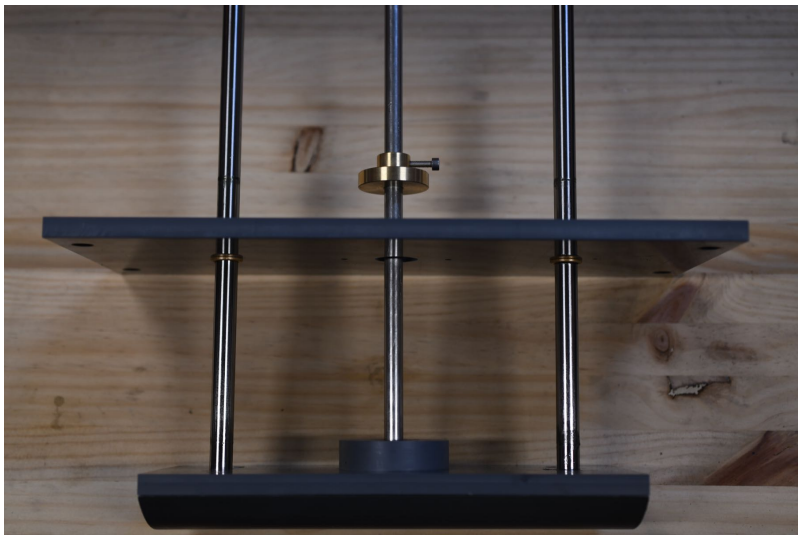

Figure 3.2: Structure manufactured for the implemented experiments

Initially, the structure was going to be controlled by means of a stepper motor working as a linear actuator. However, it was later encountered that the maximum velocity attainable by this mean was insufficient to reproduce the impact phenomena. Therefore, a free-fall procedure was employed to generate the desired impact velocity. The test structure can be seen mounted in the wave flume's test section in fig. 3.3.

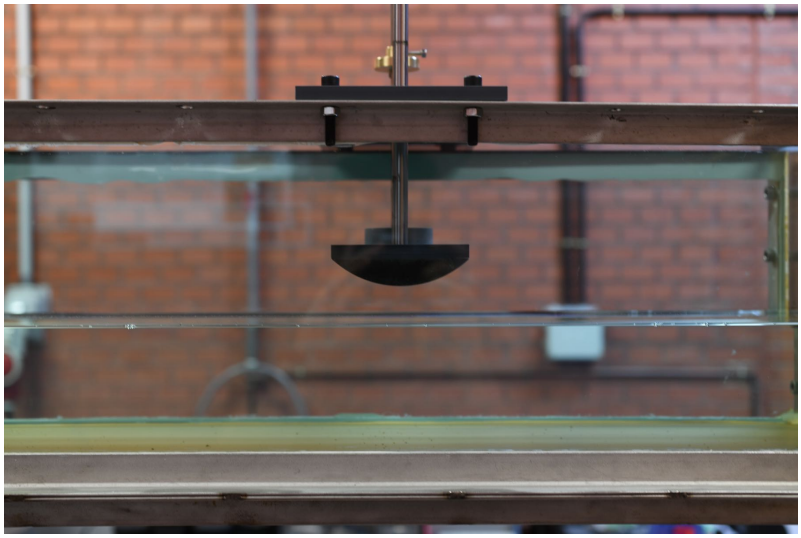

Figure 3.3: Experiment structure mounted in the wave flume's test section

Additionally, the lack of buoyancy of the solid cylinder portion forced to make use of a brass collar as a stopping mechanism (see fig. 3.4), otherwise, it would impact the bottom of the test section. This piece also served as a limit such that the flow would be affected as least as possible by the actual shape of the cylinder portion. As it can be seen in section 4.2.1, the numerical simulations were implemented with a complete circular region for the sake of simplicity and for reducing computational time. Placing the mentioned stopping mechanism on the actual experiment ensured that dynamic similarity was conserved as much as possible.

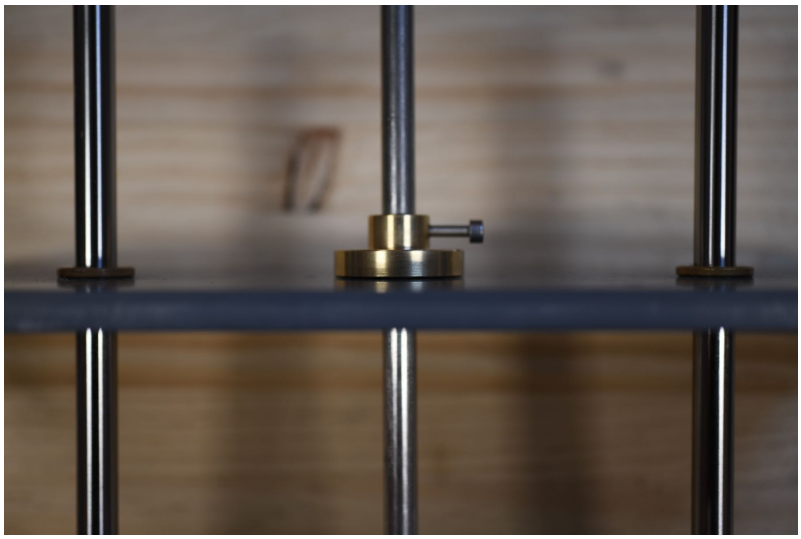

Figure 3.4: Brass collar used as a stopping mechanism

3.2 Experiments

Water level (h_0) was maintained constant at 10 cm throughout all the experiments, measured from the bottom flume wall. This facilitated maintaining the ratio R/h_0 constant, thus allowing to fulfill dynamic similarity between the later developed simulations and their respective experiments.

The impact velocity of the free-fall approach was controlled by the release height and calculated by means of high speed recordings taken with a DSLR camera (Nikon D850) on every impact.

Several experiments were developed for different height from the water surface (see table 1).

Case	A	B	C	D	E	F
d_w [cm]	10	8	6	4	2	6*

Table 1: Experiments at several distances from the interface

Case F was implemented with an additional 2 kg weight on the falling structure, in order to investigate differences in velocity with weight. The release height is the same as in Case C.

Considering that the temperature on the day of the experiments at the wave flume facility was $T = 25°C$, the properties of the fluids are summarized in the following table:

ρ_{water}	997.05 $[kg/m^3]$
μ_{water}	8.891e-4 $[Pa \cdot s]$
ρ_{air}	1.184 $[kg/m^3]$
μ_{air}	1.837e-5 $[Pa \cdot s]$

Table 2: Water and air properties at $T = 25°C$

Finally, the flow generated in these experiments can be assumed to be two-dimensional, as the test section walls do not allow variations in the direction perpendicular to them. Additionally, the cylinder solid section spanned for the whole width, i.e., its longitude is the same as the width of the test section.

3.3 Post-processing of the interface and the motion of the solid

Slow motion recordings were taken with the aforementioned camera in order to track the evolution of the free surface due to the impact. A white light screen was placed on the background to eliminate flickering in the films, and their post processing was done by means of the programs *ImageJ* and *MATLAB*.

ImageJ was used to track the evolution in time of the solid. With this information, *MATLAB* was then used to obtain the plots for such evolution. Additionally, *Polyfit*, an in-built *MATLAB* function, was used to approximate the experimental data as it will be explained in section 5.1. *ImageJ* was also used to obtain the spatial and temporal scales from the movies of the experiments, and thus compare the interface evolution with the one from the simulations.

4 Numerical analysis of a cylinder impacting a water surface

In this chapter, the impact of a solid is studied using the CFD software *Basilisk*.

Basilisk is an open-source software conceived to be the successor of *Gerris* and developed by the same authors. It first appeared in the publication "A quadtree-adaptive multigrid solver for the Serre-Green-Naghdi equations" [25]. Although based on the same principle than its predecessor, adaptive mesh refinement, it is written in a slight variant of the C programming language.

Basilisk can be considered a compiler, as it is a software in charge of compiling the program coded in C. The extension of the C programming language required to develop specific discretization schemes as well as the current solvers and functions available can be found on its website [30, 31].

4.1 *Basilisk* features

Basilisk is a program designed to solve partial differential equations on adaptive Cartesian meshes. The key aspect within this software is that fluid volumes used to discretize the fluid domain are coordinated hierarchically as a quadtree structure. Such architecture has been widely investigated for image processing and its adaptivity makes it noteworthy for conveniently generalizing schemes implemented on Cartesian meshes.

The spatial domain is discretized in square cells or cubes (in 3D). One cell might be the *parent* of up to four *children* cells (eight in 3D). Quadtree structures (octrees in 3D) basically compare data sets based on the information immediately surrounding the observed cell. Each cell has a neighbouring one at the same level in each direction (four in 2D and six in 3D). The level of a cell is determined starting from zero for the *root cell* and adding one for every group of four *children*. The *root cell* has no *parent cell* and a *leaf cell* is such that it has no *children*. The general arrangement of this discretization can be seen in fig. 4.1 and an example in fig. 4.2.

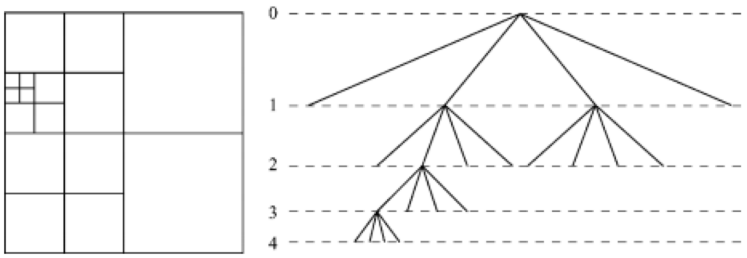

Figure 4.1: General arrangement of quadtree discretisation and corresponding tree representation [16]

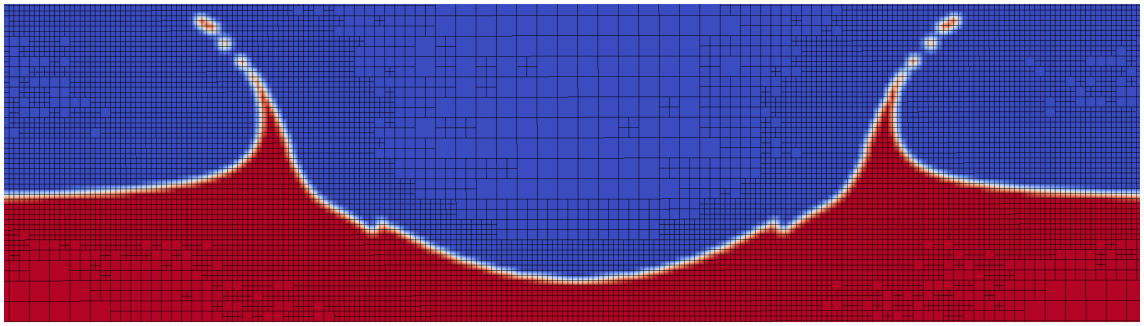

Figure 4.2: Example of quadtree discretisation

AMR algorithms are established on adjusting the spatial discretization to follow the scale and temporal evolution of flow structures. In *Basilisk*, the refinement level is controlled by means of the function *adapt_wavelet()*. Whenever the wavelet-estimated discretisation error of the fields chosen is larger than the tolerance imposed, the mesh is refined down to the maximum level specified. This can be better appreciated in section 4.2.1, where the code used for this project is discussed.

Boundary conditions are defined on the limits of the mesh. The quadtree structure actually extends beyond such limits in order to ensure consistency of regular stencils. These cells located immediately beyond the boundaries of the grid are called *ghost cells* and they take a value approximated from the desired one of the boundary conditions. Stencils are geometrical arrangements of a group of nodes in a grid that relate to the point of interest using numerical approximation routine. These arrangements are fundamental to solve PDEs numerically.

As mentioned in [25, section 3.6], "the decoupling between the low-level implementation of different types of grids from the numerical scheme itself allows the independent development of optimized low-level strategies". This is the main differentiating factor between *Basilisk* and *Gerris*. Additionally, the performance gain over the same scheme implemented in *Gerris* is substantial, running approximately eight times faster.

4.2 Simulation analysis

4.2.1 Description of the code implemented in *Basilsik*

The code implemented to simulate the experiments is presented and explained in this section. This will serve as an introductory guide for future works based on this project.

First, the numerical schemes to be used in the code were established by calling their respective libraries (see fig. 4.3).

```
1 //////////*NUMERICAL SCHEMES*//////////
2 #include "navier-stokes/centered.h"
3 #include "two-phase.h"
4 #include "navier-stokes/conserving.h"
5 #include "fractions.h"
6 #include "reduced.h"
7 #include "vtk.h"
8 //////////*-----------------*//////////
```

Figure 4.3: Code segment: numerical schemes

Next, some global variables were defined to easily arrange the code. Mainly, the refinement level, the Froude and Reynolds numbers, the timestep of the outputs, and the simulation time (see fig. 4.4).

```
11 //////////*GLOBAL VARIABLES*//////////
12 int MAXlevel = 9; // Maximum refinement level of the mesh
13 int MINlevel = 6; // Minimum refinement level of the mesh
14
15 double REYNOLDS = 109073.66;
16 double FROUDE = 1.135;
17
18 double OUTdt = 0.01;
19 double t_end = 5.;
20
21 scalar f0[]; /*Initial water level*/
22 scalar cylinder[];
23 scalar m[];
24 //////////*----------------*//////////
```

Figure 4.4: Code segment: global variables

Essentially, two types of function structures are found in the code, *main* and *event* functions.

As previously stated, the timestep used to integrate numerical schemes may vary as the simulation evolves due to stability requirements. *event* functions ensure that the demanded action takes place exactly when and as many times as specified. The *event* function is analogous to *for* loops in C, as their syntax is similar. However, the former is more flexible as certain conditions of the structure may be omitted.

The *main* function is original from C, where the setup is performed. Fluid properties and gravity are defined based on the non-dimensional form of the code. Additionally, the domain is defined as well as the the initial mesh refinement level (see fig. 4.5). The function "s.refine = s.prolongation = fraction_refine;", lets the code know that the initial water level (f0) is a volume fraction field.

```
27 //////////*MAIN*//////////
28 int main(){
29
30   /*WATER*/
31   rho1 = 1.;
32   mu1 = 1./REYNOLDS;
33
34   /*AIR*/
35   rho2 = 1.184/997.05;
36   mu2 = (1.837e-5/8.891e-4)*mu1;
37
38   L0 = 3.5;
39   origin (-1.75, -3.2);
40
41   init_grid (1 << MAXlevel);
42
43   for (scalar s in {f0})
44     s.refine = s.prolongation = fraction_refine;
45
46   G.y = - 1./sq(FROUDE);
47   run();
48
49 }
50 //////////*----*//////////
```

Figure 4.5: Code segment: main function

As mentioned in section 2.1, boundary conditions for the left, bottom and right walls of the domain were characterized as solid walls with no penetration, i.e., defining Dirichlet BC for the local normal velocity component equal to zero. The top wall was characterized as an outflow boundary, i.e, defining a Dirichlet BC for the pressure field equal to zero (reproducing the external atmosphere) and a Neumann BC for the derivative normal to the wall of the velocity equal to zero (see fig. 4.6).

```
53 //////////*BOUNDARY CONDITIONS (DOMAIN)*//////////
54 u.n[top]  = neumann(0.);
55 p[top]    = dirichlet(0.);
56 pf[top]   = dirichlet(0.);
57 //////////*--------------------------*//////////
```

Figure 4.6: Code segment: boundary conditions on the domain

Initial conditions were established afterwards, fig. 4.7. The *fraction()* function defines a volume fraction field directly from a function; in this case, it defines the initial position of the water level (interface). Function *foreach()* iterates over all the stencils defining the discretized tracer field (f). Finally, function *boundary ()* updates ghost cells when the values inside the domain are modified and before any operation on stencils.

```
60 //////////*INITIAL CONDITIONS*//////////
61 event init (t = 0.) {
62
63   fraction (f0, -2.1-y);
64     foreach() {
65       f[] = f0[];
66     }
67     boundary ({f});
68
69 }
70 //////////*------------------*//////////
```

Figure 4.7: Code segment: initial conditions

The next event (*moving_cylinder*) defines the movement of the cylinder, i.e., the BC on the solid (see fig. 4.8) . The geometry could have been imported from a *.stl* file [37], but given the simplicity of the studied geometry, the fraction field of the solid was conveniently written as the mathematical expression of a circle. The center of the cylinder moves, in every iteration of the solver, the distance given by $(v_{c,x} \cdot t)$ and $(v_{c,y} \cdot t)$ along x and y direction respectively. The scalar field *cylinder* is then delimited as a solid volume fraction field where the velocity field can be imposed as a volume-weighted average. With this simple approach the flow is forced to move in order to fulfill the imposed condition that inside the cylinder fraction field, the velocity must be equal to the desired velocity (vc). Two velocities were defined within this event in order to represent more accurately the results obtained in the experiments. The first velocity corresponds to the non-dimensional impact velocity, i.e., $U^* = 1$, whereas the second one represents the complete stoppage of the solid, which is discussed in section 5.

```
73 //////////*BOUNDARY CONDITION (SOLID)*//////////
74 event moving_cylinder (i++) {
75
76   if(t<1.31){
77       coord vc = {0.,-1};
78       fraction (cylinder, - (sq(x - (vc.x*t)) + sq(y - (vc.y*t)) - sq(1.)));
79       foreach(){
80       foreach_dimension(){
81         u.y[] = cylinder[]*vc.y + (1. - cylinder[])*u.y[];
82       }
83     }
84     boundary ((scalar *){u});
85   }
86
87   else {
88     coord vc = {0.,0.};
89       fraction (cylinder, - (sq(x - (vc.x*t)) + sq(y - (-1.31+vc.y*t)) - sq(1.)));
90       foreach(){
91       foreach_dimension(){
92         u.y[] = cylinder[]*vc.y + (1. - cylinder[])*u.y[];
93       }
94     }
95     boundary ((scalar *){u});
96   }
97 }
98 //////////*------------------------*//////////
```

Figure 4.8: Code segment: boundary condition on the solid

It should be noted that, although this condition does not strictly fulfill the no penetration BC, it is still a remarkable and efficient way to implement it. In order to be strictly accurate, an *embedded boundary* approach should be used, as it is observed in section 6. Nonetheless, the approach followed served altogether to reproduce the phenomena as it will be discussed in section 5, while the errors introduced are of the same order as those introduced by the spatial discretization scheme. A similar approach is used in [39].

As explained in section 4.1, AMR is required every iteration based on the accuracy of both the velocity and tracer fields, which can be seen in fig. 4.9.

```
101 //////////*ADAPTIVE MESH REFINEMENT*//////////
102 event adapt (i++) {
103
104   double uemax = 0.01;
105   double femax = 0.01;
106
107   adapt_wavelet ((scalar *){u,f}, (double[]){uemax,uemax,femax}, MAXlevel, MINlevel);
108
109 }
110 //////////*------------------------*//////////
```

Figure 4.9: Code segment: wavelet-estimated convergence criterion

Finally, the remaining events serve to obtain some convergence statistics (fig. 4.10), as well as output data for post-processing (figs. 4.10, 4.12 and 4.13).

```
113 //////////*CONVERGENCE STATISTICS*//////////
114 event logfile_terminal (i++){
115
116   fprintf (stderr, "%d %d %g %d %d %d %d\n", i, N, t, mgp.i, mgp.nrelax, mgu.i, mgu.nrelax);
117
118 }
119 //////////*----------------------*//////////
```

Figure 4.10: Code segment: convergence statistics

```
122 //////////* OUTPUT (TRACER FIELD MOVIES)*//////////
123 event images (t += OUTdt; t <= t_end) {
124
125   foreach(){
126     m[] = 0.5 - cylinder[];
127   }
128   boundary ({m});
129
130   output_ppm (f, file = "TracerField.mp4", box = {{-1.73,-3.06625},{1.73,-1.12}}, linear = false, min = 1, max = 0, mask = m);
131
132 }
133 //////////*--------------------------*//////////
```

Figure 4.11: Code segment: tracer film (output)

```
136 //////////* OUTPUT (.vtk FILES)*//////////
137 #if 1
138 event outvtk  (t = 0.; t <= t_end; t+=OUTdt) {
139   scalar * list;
140
141   bool linear;
142
143   char name[80];
144
145   sprintf (name, "ParaviewAt-%04g-Seconds.vtk", t);
146
147   dump (file = name);
148
149   FILE * fpvtk = fopen(name, "w");
150
151   scalar omega[];
152
153   vorticity (u, omega);
154
155   output_vtk (list = {f, m, p, u.x, u.y, omega}, N, fpvtk, linear = true);
156
157   fclose (fpvtk);
158 }
159 #endif
160 //////////*-------------------*//////////
```

Figure 4.12: Code segment: .vtk files (output)

```
164 //////////* OUTPUT (.gfs FILES)*//////////
165 #if 1
166 event gfsview (t = 0.; t <= t_end; t+=OUTdt) {
167
168   char name[80];
169
170   sprintf (name, "GerrisAt-%04g-Seconds.gfs", t);
171
172   dump (file = name);
173
174   FILE * fpgfs = fopen(name, "w");
175
176   output_gfs (fpgfs);
177 }
178 #endif
179 //////////*-------------------*//////////
```

Figure 4.13: Code segment: .gfs files (output)

4.2.2 Schemes summary

Numerical schemes can be regarded as algebraic relations between the values of variables in adjacent grid points. The main scheme to be used is "navier-stokes/centered.h" [32], which approximates numerically the incompressible, variable density Navier-Stokes equations, eqs. (2.5) and (2.6).

The *centered.h* library uses *Bell-Collela-Glaz* advection scheme [33] and an implicit viscosity solver. The timestep is limited by the CFL condition, shown for the two-dimensional case in eq. (4.1). It is a necessary condition for convergence when solving certain PDEs numerically, otherwise the physical characteristic time within the numerical simulation would be smaller than the timestep used to study the evolution and, thus, information would be lost, leading to a wrong solution or not even converging.

$$C = \Delta t \left(\sum_{i=1}^{n} \frac{u_{x_i}}{\Delta x_i} \right) \leq C_{max} \tag{4.1}$$

Library *two-phase.h* [34] facilitates the arrangement for flows with two immiscible fluids. The fluid properties can then be easily defined, mainly the density and viscosity, for both fluids. The interface between the two fluids is tracked with a VOF method, where the volume fraction f is defined as the ratio of volume occupied by the fluid to the total volume of the cell. This volume fraction takes the value $f = 1$ for one fluid and $f = 0$ for the other.

Additionally, the *conserving.h* [35] file implements conservation of momentum of the velocity components, a critical feature to ensure stability of the solver for the air-water density ratio configuration. Finally, *reduced.h* [36] redefines the gravity as an interfacial flow.

4.2.3 Analysis of mesh refinement

Convergence of simulation results with mesh refinement level is presented in this section. Water depth at a certain location and instant was chosen as a reference parameter to study this convergence. In particular, *Case E* was used for this analysis. The water level was measured for three refinement levels at 12 [cm] from the initial vertical symmetry plane and at the instant $t = 0.125[s]$, $t^* = 0.72[-]$. The snapshots of the tracer field used for this measurement can be seen in figures 4.14, 4.15 and 4.16. In all of these, the solid was removed for a clearer depiction.

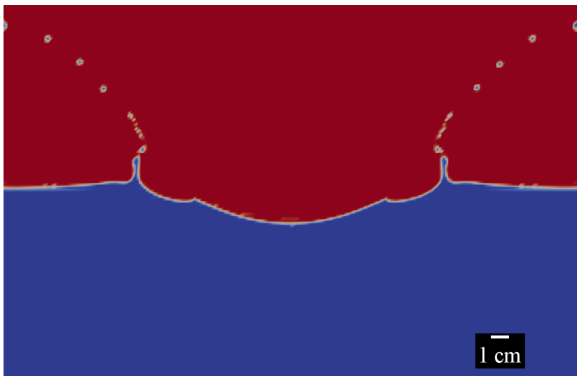

Figure 4.14: Water level of *Case E* at $t = 0.125[s]$, $t^* = 0.720[-]$ with a refinement level of **8**

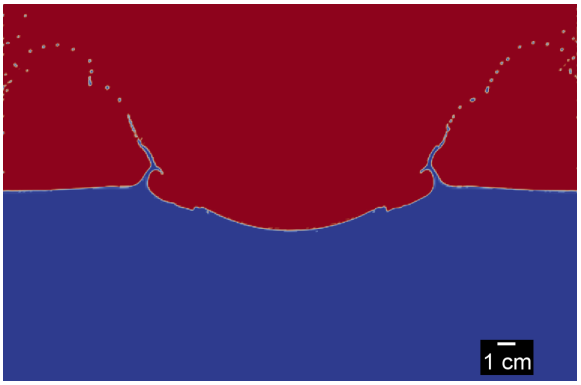

Figure 4.15: Water level of *Case E* at $t = 0.125[s]$, $t^* = 0.720[-]$ with a refinement level of **9**

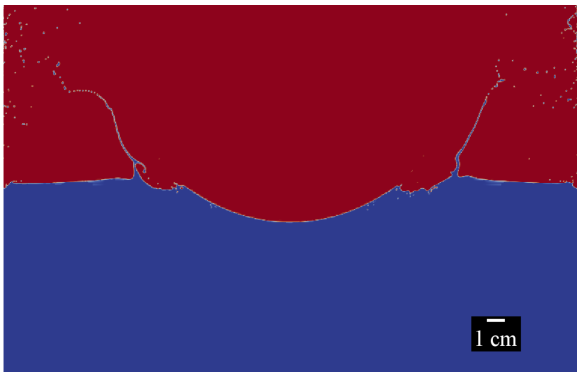

Figure 4.16: Water level of *Case E* at $t = 0.125[s]$, $t^* = 0.720[-]$ with a refinement level of **10**

The results for the measurements are presented in table 3.

Max refinement level	8	9	10
Water level [cm]	10.39	10.52	10.51

Table 3: Water level for different refinement levels measured at 12 [cm] from the symmetry plane

It is worth noting that the results converge when increasing the maximum refinement level. Computational time for different refinement levels is presented for cases *A* and *E* in table 4, as these will be the main cases discussed in section 5.2.

Max refinement level	8	9	10
Case A	550 [s]	10070 [s]	62050 [s]
Case E	124 [s]	4180 [s]	32160 [s]

Table 4: Computational time for different cases and different levels of refinement

Taking all this into account, it becomes clearer that maximum level of refinement equal to 9 represents a fair trade off between computational cost and accuracy in the results.

Furthermore, after examining several problems on the *Basilisk* website with similar complexity to the one proposed in this project, a noteworthy example is found [38]. In this case a three dimensional two-phase flow around a boat is studied. After analyzing the refinement used, a level 9 is found. Therefore, additional evidence is provided on the fact that a level 9 of refinement is significantly high to provide accurate results and in an efficient way, as computational time is considerably lower than higher levels.

5 Results and Discussion

The results of the project are presented in this section. Priority is given to experimental *Case E* and *Case A* (see table 1), as they represent the extreme cases. Results for the other cases are also presented.

5.1 Experimentally determined trajectory of the impacting body

First of all, the experimental cases were post-processed as presented in section 3.3. In figures 5.6 to 5.1, the experimental height evolution of the solid is presented for each case. The origin was placed at the impact instant as it provides a clearer depiction of the length and time scales.

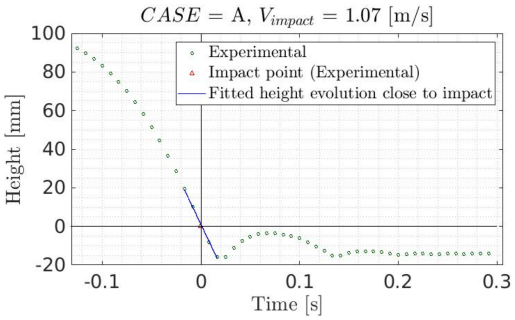

Figure 5.1: Height evolution for $d_w = 10cm$

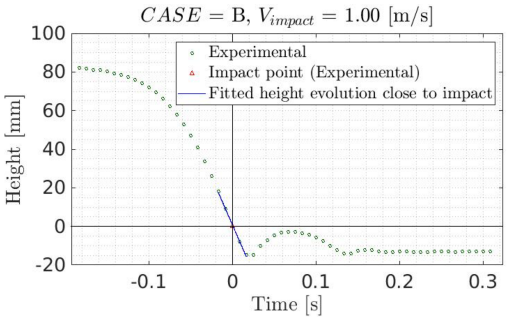

Figure 5.2: Height evolution for $d_w = 8cm$

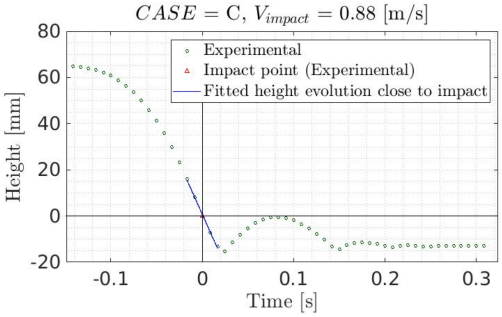

Figure 5.3: Height evolution for $d_w = 6cm$

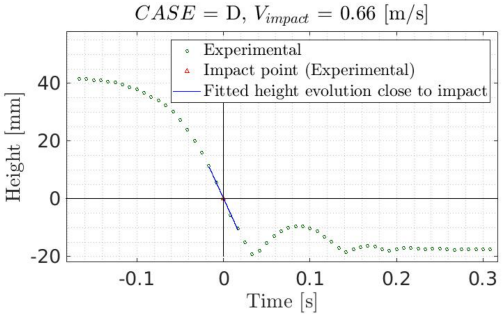

Figure 5.4: Height evolution for $d_w = 4cm$

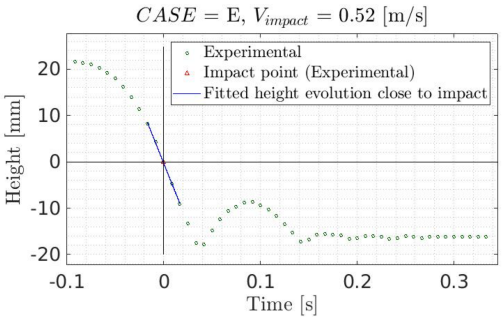

Figure 5.5: Height evolution for $d_w = 2cm$

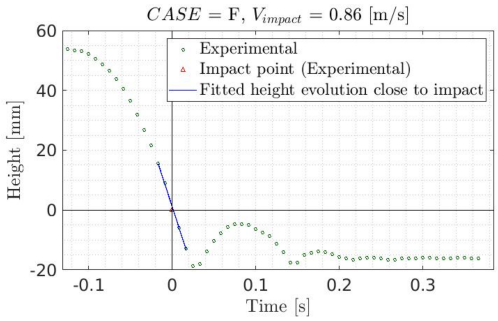

Figure 5.6: Height evolution for $d_w = 6cm + 2kg$ extra

Similar behaviours can be observed throughout the cases, although different spatial ranges are covered in each case. It can be be seen how their respective distance is covered before impacting onto the water surface. However, a small difference with respect to the intended distance from the water interface can be appreciated on the actual initial position of the cylinder. This was due to the hand-held release approach carried out in the experiments. Moreover, the cylinder section did not penetrate the initial water level more than 20 [mm] in all the cases. This had to do with the position at which the collar-stop was placed and for the reasons mentioned in section 3.1.

Additionally, it was observed that the solid initially accelerated from rest to an almost constant value of the velocity. Inspecting the graphs nearby their respective impact points, it was assumed that the solid entered the water approximately with a constant velocity in all cases. In fact, the temporal height evolutions are accurately represented by first order polynomials nearby their respective impact points. Therefore, the velocity can be indeed assumed to be constant nearby this region.

From the point where the height reaches the maximum negative value, the validity of the experiment to describe the physical phenomena of applications mentioned in section 1.1 is decreased. Exactly at that point, the brass collar located in the central shaft as a stopping mechanism impacted the upper plate of the structure. As explained in section 3.1, this mechanism was necessary to carry out the experiments.

Despite this discrepancy with impacts of buoyant structures, the monotonic decrease in the amplitude of the oscillations of the height illustrates a damping motion. The nature of this motion, although induced by the bounce of the brass collar on the upper plate, serves as a similar behaviour of vertical impacts once the impact interval has passed and the structure is floating until complete stoppage is reached.

As it was expected, additional weight placed on the structure had negligible effects on the impact velocity. In figures 5.3 and 5.6, although having the same release height and different weights, the additional mass did not increase the impact velocity. In fact, the evolution profiles obtained are highly similar as temporal and spatial scales coincide with a large degree of accuracy. Therefore, physical similarity is proved, which means that the falling speed does not depend on the weight. The minimum height value is reached approximately at $0.02[s]$, the subsequent maximum recovery height reached at $0.08[s]$ and so on. This similarity was expected considering that the experiments carried out were fundamentally *Galilean* free-falls.

5.2 Comparison of experiments and simulations

In this section, the validation of the CFD model is approached from the point of view of interface evolution comparison. As mentioned in section 3.2, dynamic similarity was easily fulfilled by maintaining constant the ratio R/h_0 among the experiments and simulations, as it was necessary to be able to compare them.

As advanced in section 2.1, and presented in section 4.2.1, the Reynolds and Froude numbers where computed for each test case and then introduced in the code to simulate them.

Reproducing the instants immediately surrounding the impact time was the main objective of the simulations. Taking into account the findings presented in section 5.1, a constant entry velocity was assumed. This allowed to simplify considerably the numerical code, and at the same time, achieve a significant degree of accuracy with regard to the experiments. Once the impact velocities were calculated, the Reynolds and Froude numbers were also computed for each experimental case (see table 5).

Case	*A*	*B*	*C*	*D*	*E*	*F*
U [m/s]	1.071	0.996	0.884	0.656	0.523	0.862
Re	109073.75	101454.76	90082.30	66767.99	53133.27	87852.62
Fr	1.135	1.055	0.937	0.694	0.553	0.914

Table 5: Experimental values for the impact velocities U, Reynolds and Froude numbers of each experiment

The values obtained for both the Reynolds and Froude numbers in the experiments have a smaller order of magnitude than the ones that would be obtained in real ditching scenarios. Nonetheless, *Case A* could still be compared with a low speed water-impact event, e.g., spacecraft splashdown with parachutes. Also, the values for *Case C* and *Case F* are very similar. As explained before, the added mass did not have a significant effect on the impact velocity, thus the difference appreciated between such values is due to the accuracy of the image analysis software and the method used to obtain them. This small difference in the calculated impact velocity generates the discrepancy in the values of the Reynolds and Froude numbers. However, they are still of the same order of magnitude, thus reinforcing the statement that adding weight does not influence the impact velocity for the experiments considered.

Given that the impact velocity could be considered constant, the imposed velocity of the cylinder (see section 4.2.1) greatly simplified its implementation in the code, still yielding significant results.

5.2.1 Interface comparison for *Case E*

The evolution of the experimental and simulated interfaces of *Case E* is presented in the following figures. Comments are made as the evolution progresses.

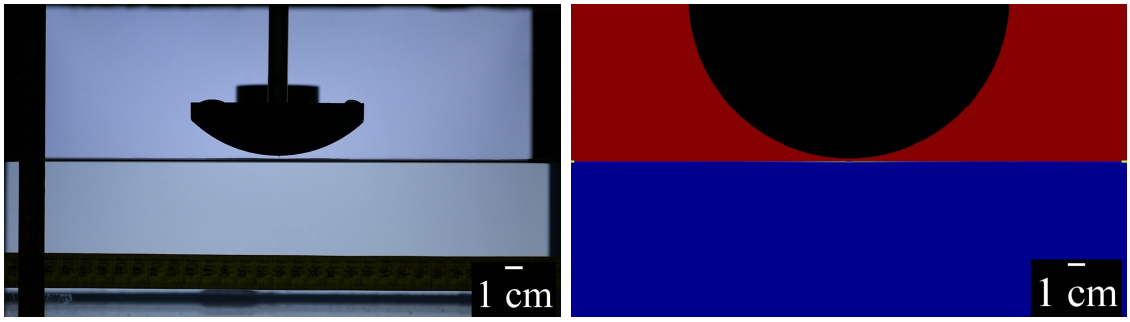

Figure 5.7: *Case E* at $t = -0.01[s]$, $t^* = -0.058[-]$

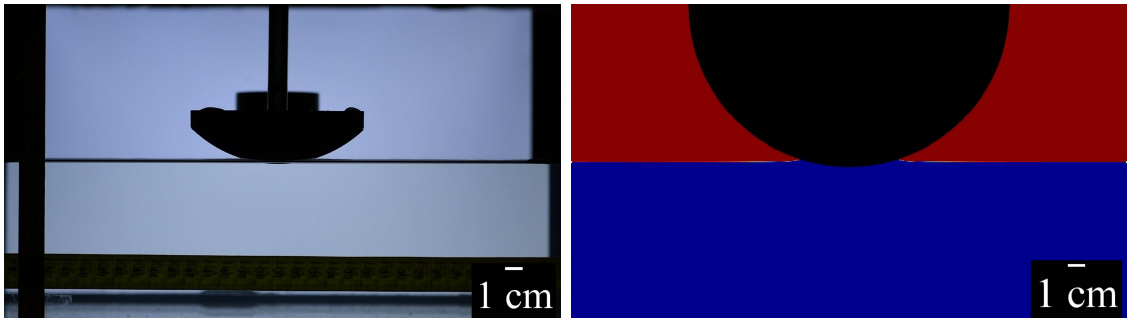

Figure 5.8: *Case E* at $t = 0.000[s]$, $t^* = 0.000[-]$

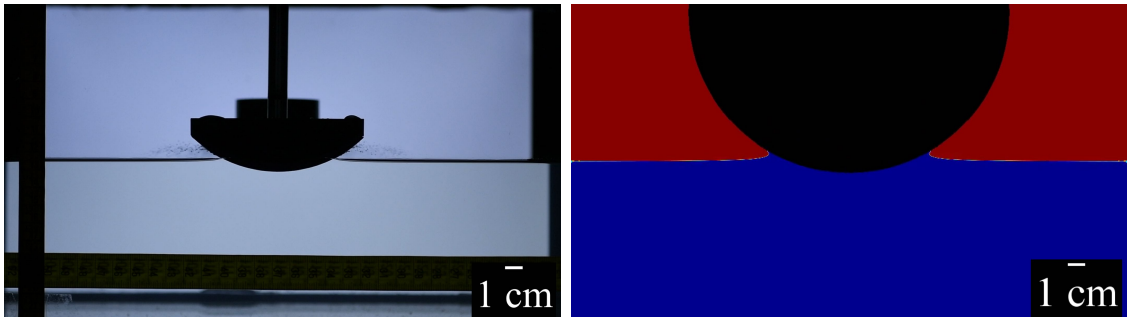

Figure 5.9: *Case E* at $t = 0.008[s]$, $t^* = 0.046[-]$

Up to this instant any significant difference on the interface can be appreciated, as it was expected from such early stages. However, in fig. 5.9, there appears to be some spray phenomena in the experiment. The numerical simulation is not fine enough to simulate the atomization of the liquid sheet ejected upon the impact. Moreover, the dynamics of this sheet is intrinsically 3D, and thus cannot be captured by a 2D simulation.

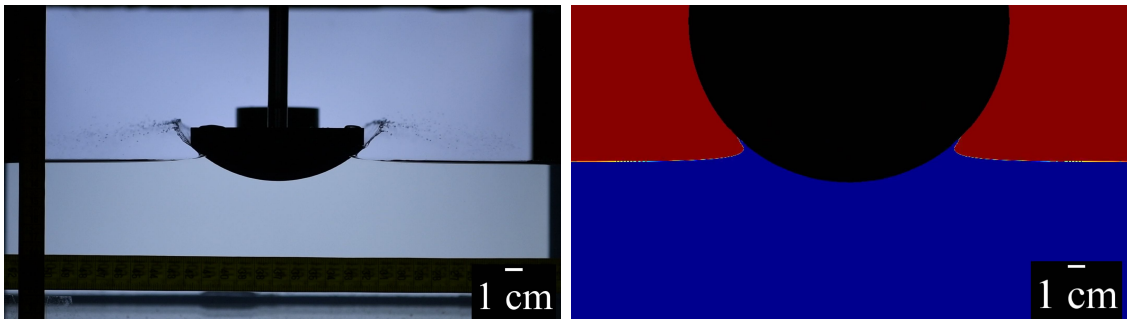

Figure 5.10: *Case E* at $t = 0.018[s]$, $t^* = 0.104[-]$

In fig. 5.10, the water flow adhered to the falling solid in the experimental case interacted with the edges. Although the stopping mechanism was placed such that the cylinder section would stop before entering fully, some spilling due to this encounter still took place.

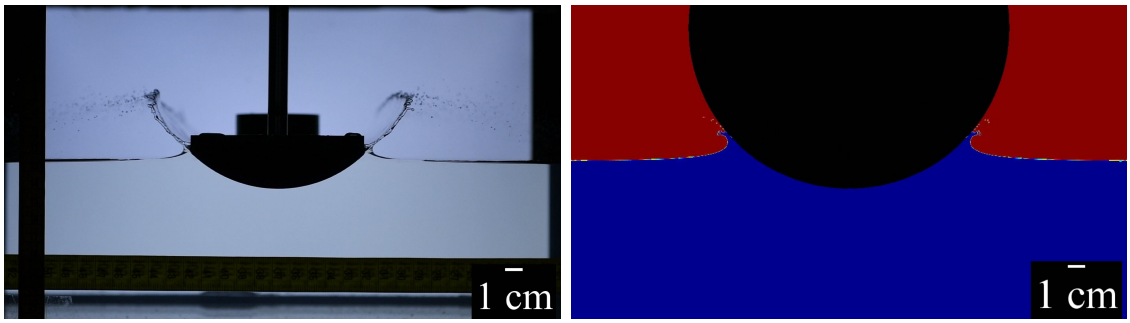

Figure 5.11: *Case E* at $t = 0.025[s]$, $t^* = 0.144[-]$

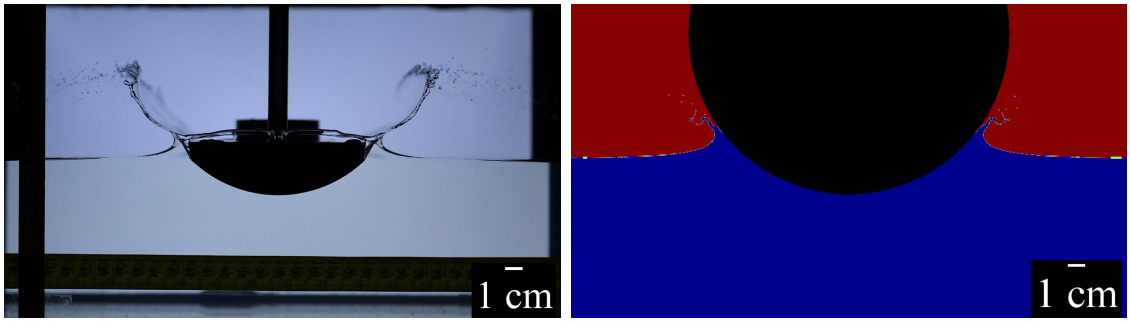

Figure 5.12: *Case E* at $t = 0.033[s]$, $t^* = 0.190[-]$

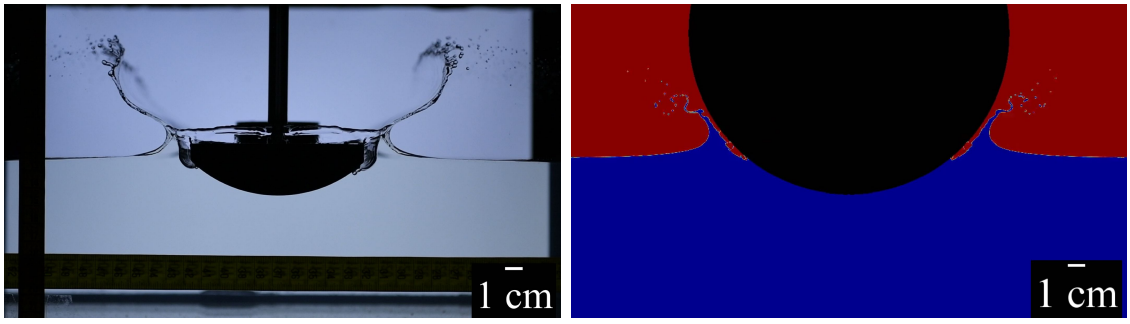

Figure 5.13: *Case E* at $t = 0.043[s]$, $t^* = 0.248[-]$

Figures 5.12 and 5.13 correspond to the first minimum height encountered by the solid, as it can be seen in fig. 5.5. As mentioned before, at this point the stopping mechanism was responsible for the bounce of the structure and the subsequent oscillatory motion of the solid on the water. In fig. 5.12 the initial superficial waves formed by the impact of the solid can be observed in both cases. In the experimental case some further spilling occurs, however, as previously mentioned, this is due to the flow encounter with the sharp edges of the cylinder section. Additionally, in fig. 5.12 the solid is still moving slightly as the flow in front remains more attached, whereas, in fig. 5.13 the solid is completely stopped. Therefore, the motion of the water is carried out by the pressure transmitted from the solid, and the flow in front of it begins to separate from that front portion. At this instant the main observed superficial waves at both lower sides of the solid begin to travel further away from it. In fig. 5.13, aeration is also observed in both simulation and experiment.

From the instant of fig. 5.13 until fig. 5.18, the experiment begins to travel upwards due to the bounce of the stopping mechanism on the upper test plate. However, as explained before, the simulation was implemented with a complete stop.

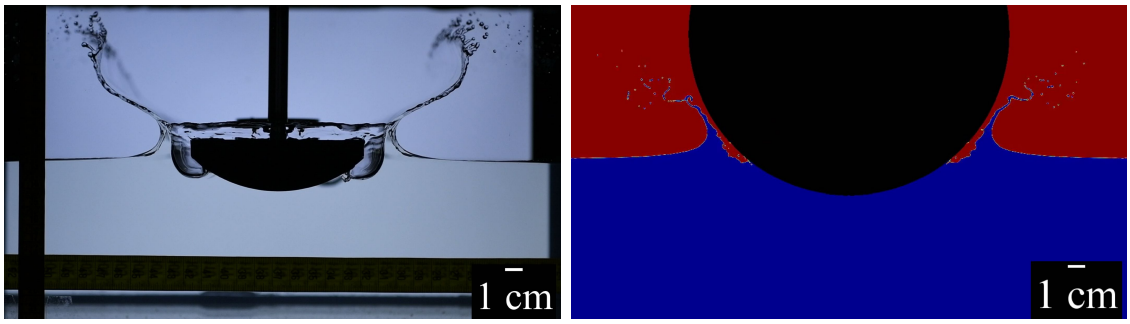

Figure 5.14: *Case E* at $t = 0.500[s]$, $t^* = 0.288[-]$

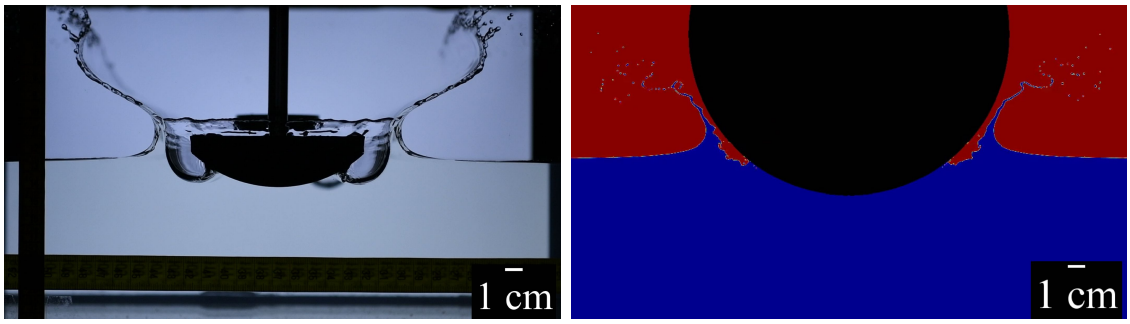

Figure 5.15: *Case E* at $t = 0.058[s]$, $t^* = 0.334[-]$

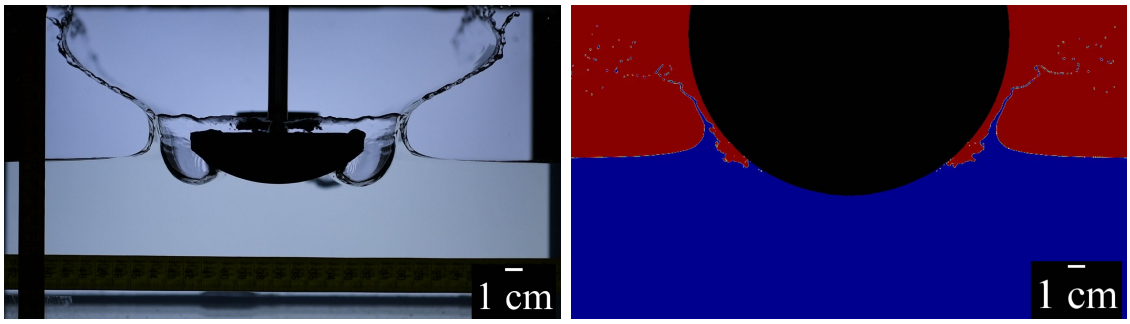

Figure 5.16: *Case E* at $t = 0.068[s]$, $t^* = 0.392[-]$

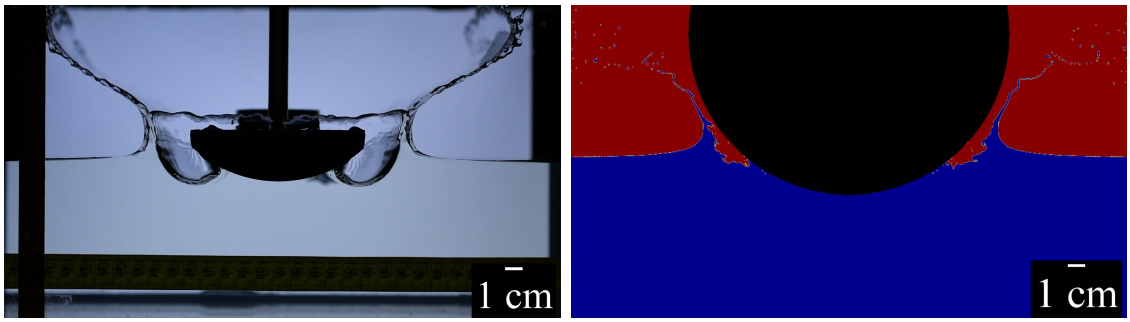

Figure 5.17: *Case E* at $t = 0.075[s]$, $t^* = 0.432[-]$

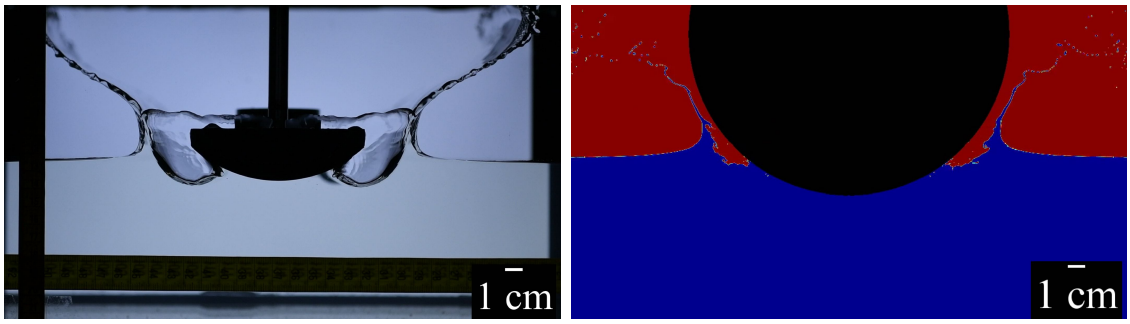

Figure 5.18: *Case E* at $t = 0.083[s]$, $t^* = 0.478[-]$

Whilst examining the interval between figures 5.13 and 5.18, the main difference arises from the fact that, in the experiment, apart from the initial downward bulk motion of the water mass (transmitted by the impact), there is an upward movement of the solid (see fig. 5.5). This introduces an additional source of flow expansion in the region immediately below the cylinder. In fact, this is the reason why the main water waves travel further away from the solid and the air gap created is larger in the experiment as time evolves in this interval. Despite this, the relative distance between these outward traveling waves and the solid still increases, only not as much as in the experimental case. Suction takes place during this time interval. As explained before, this is one of the major contributing factors to the generation of the stopping hydrodynamic force on the solid.

Furthermore, the main spilling of both waves in the experiment can be seen in the simulation. It is caused by the momentum transmitted to the liquid in the impact, which propagates away in the form of waves.

From fig. 5.19 to fig. 5.25, the cylinder section in the experiment begins its second and final major falling motion (see fig. 5.5).

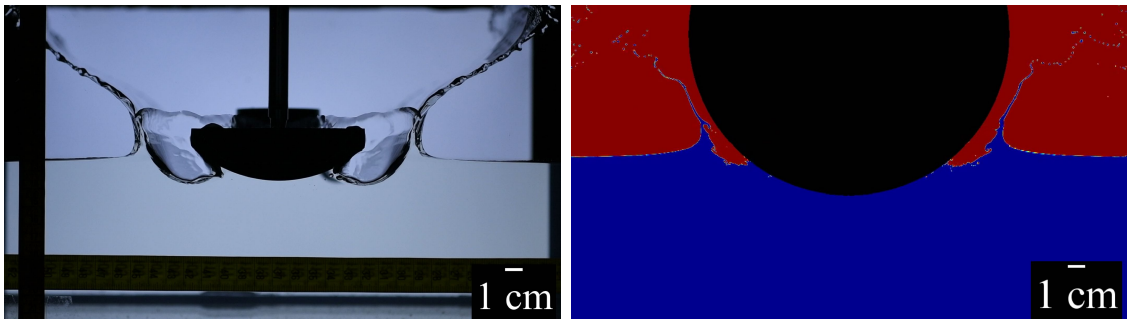

Figure 5.19: *Case E* at $t = 0.093[s]$, $t^* = 0.535[-]$

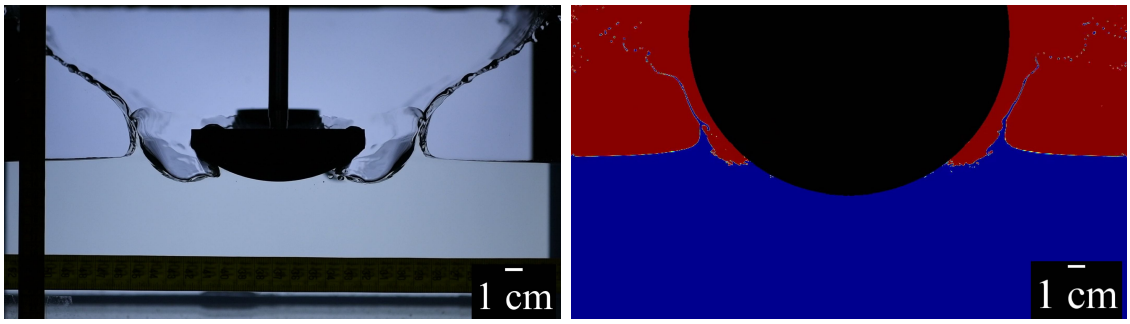

Figure 5.20: *Case E* at $t = 0.100[s]$, $t^* = 0.576[-]$

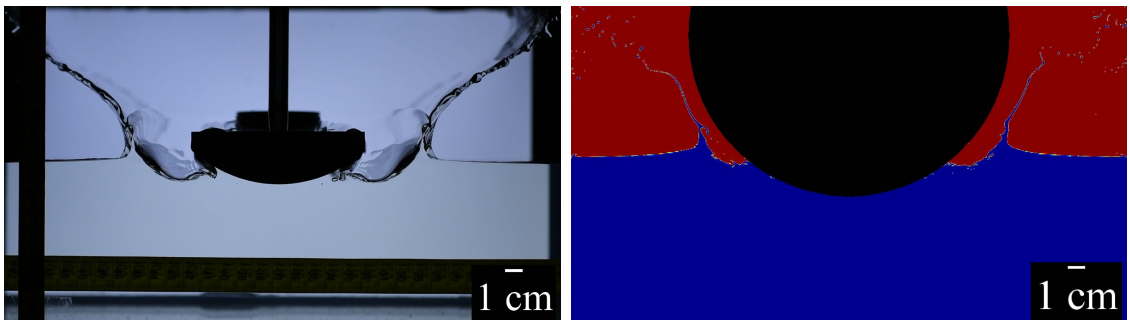

Figure 5.21: *Case E* at $t = 0.108[s]$, $t^* = 0.622[-]$

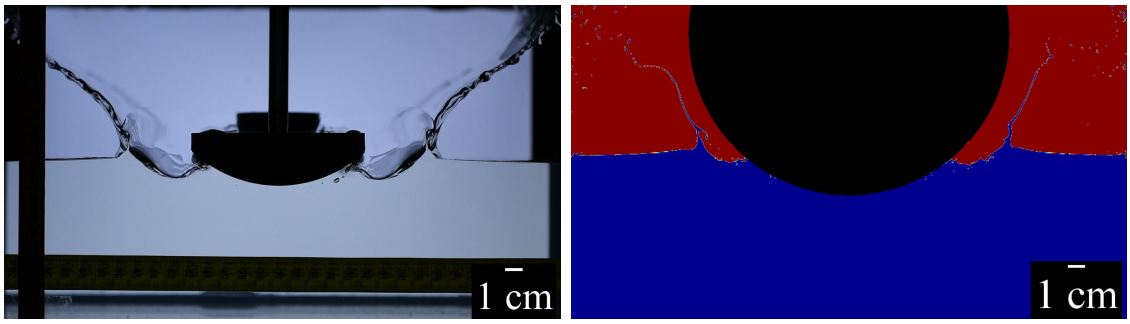

Figure 5.22: *Case E* at $t = 0.118[s]$, $t^* = 0.679[-]$

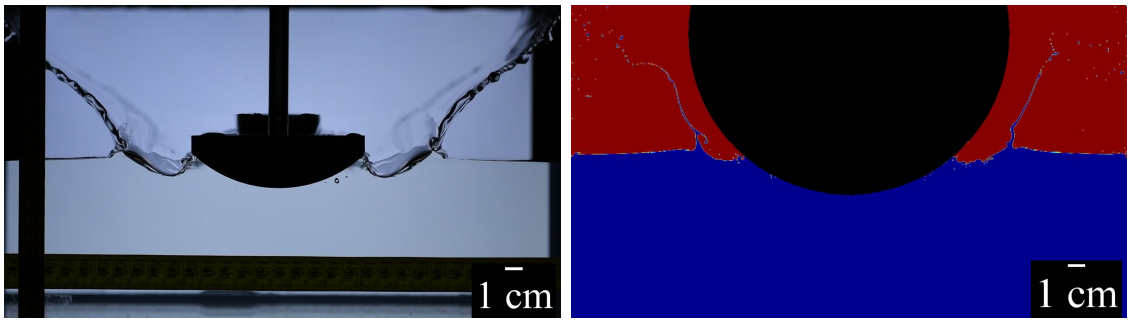

Figure 5.23: *Case E* at $t = 0.125[s]$, $t^* = 0.720[-]$

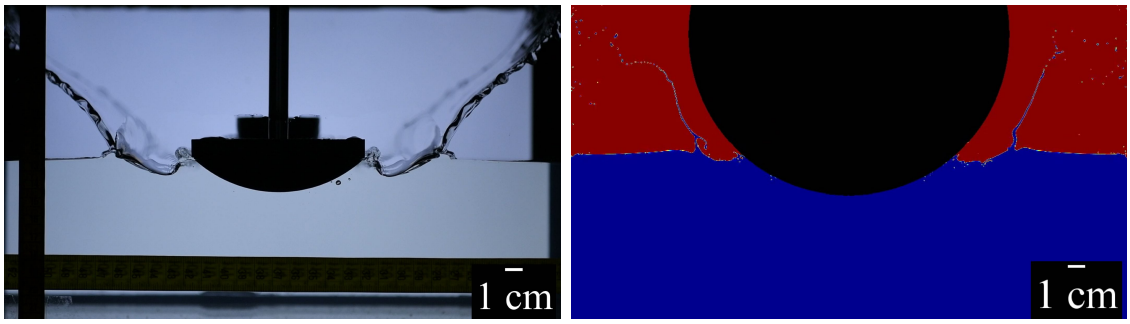

Figure 5.24: *Case E* at $t = 0.133[s]$, $t^* = 0.766[-]$

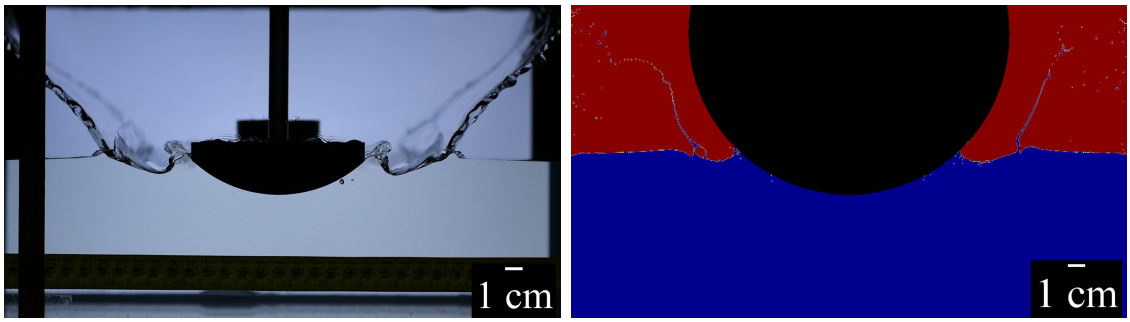

Figure 5.25: *Case E* at $t = 0.143[s]$, $t^* = 0.823[-]$

By analyzing the time interval between figures 5.19 and 5.25 the generation of two second superficial waves is observed. Here is where some limitations of the implemented code begin to arise. The main secondary falling motion of the cylinder in the experiment is observed to amplify this effect.

Nonetheless, similar superficial wave structures appear on the simulation. This indicates that the reflection of the initial wave due to the impact is one of the main originators of the discussed secondary wave structure. When the initial reflected wave encounters the solid on its upwards travelling motion, the water flow experiences a sudden change of direction due to the cylinder solid boundaries, thus, the flow gets redirected towards the sides.

Finally, from figures 5.26 to 5.39, the interface comparison for the time interval between $t = 0.150[s]$, $t^* = 0.864[-]$ and $t = 0.258[s]$, $t^* = 1.486[-]$ is presented. This interval spans from the point of minimum height of the second bounce to stoppage (see fig. 5.5).

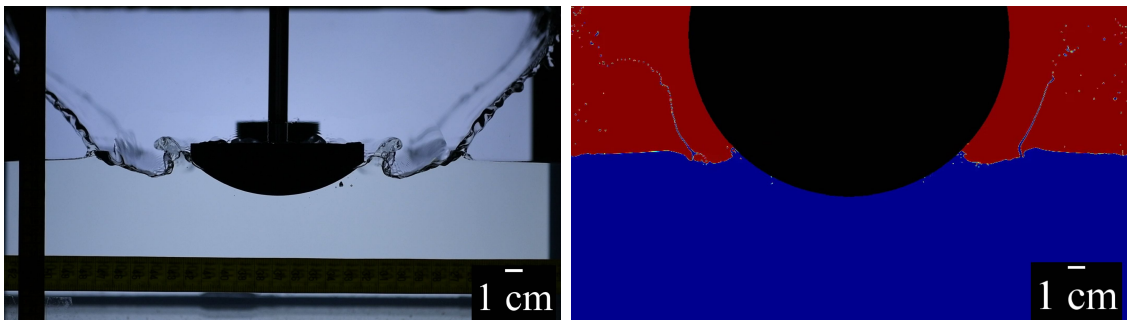

Figure 5.26: *Case E* at $t = 0.150[s]$, $t^* = 0.864[-]$

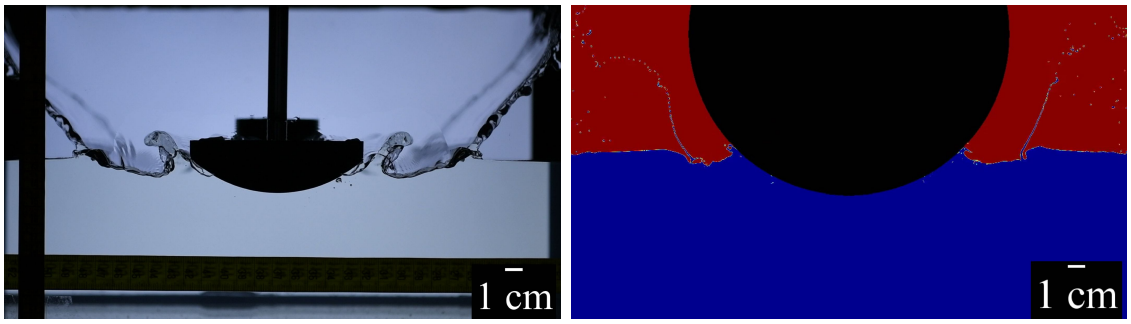

Figure 5.27: *Case E* at $t = 0.158[s]$, $t^* = 0.910[-]$

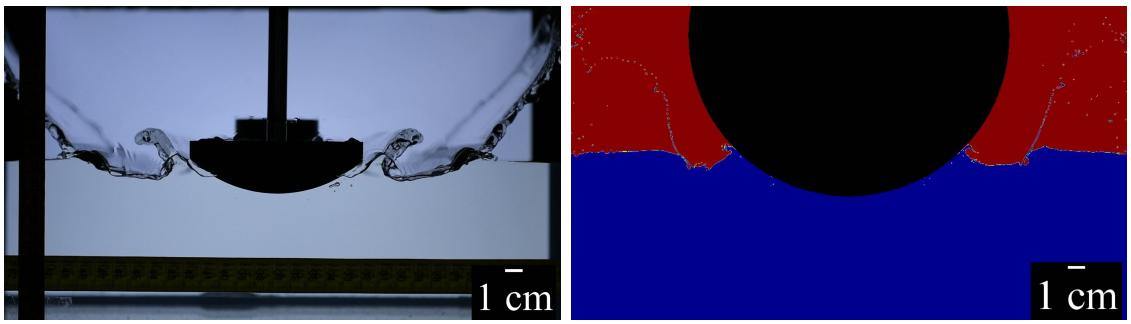

Figure 5.28: *Case E* at $t = 0.168[s]$, $t^* = 0.967[-]$

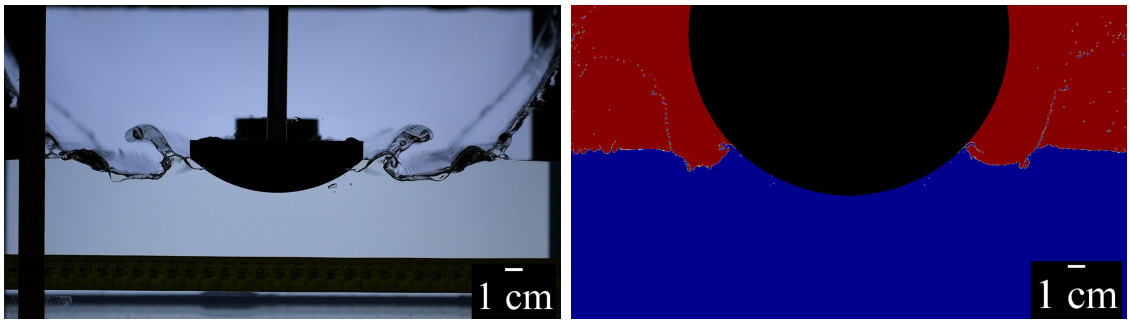

Figure 5.29: *Case E* at $t = 0.175[s]$, $t^* = 1.008[-]$

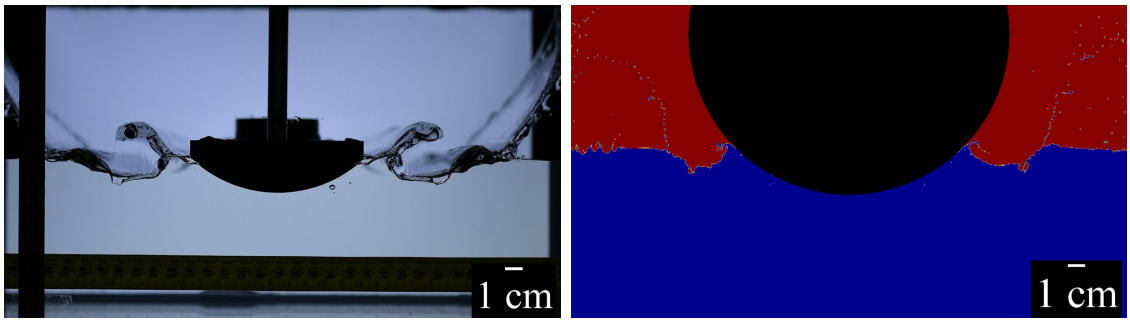

Figure 5.30: *Case E* at $t = 0.183[s]$, $t^* = 1.054[-]$

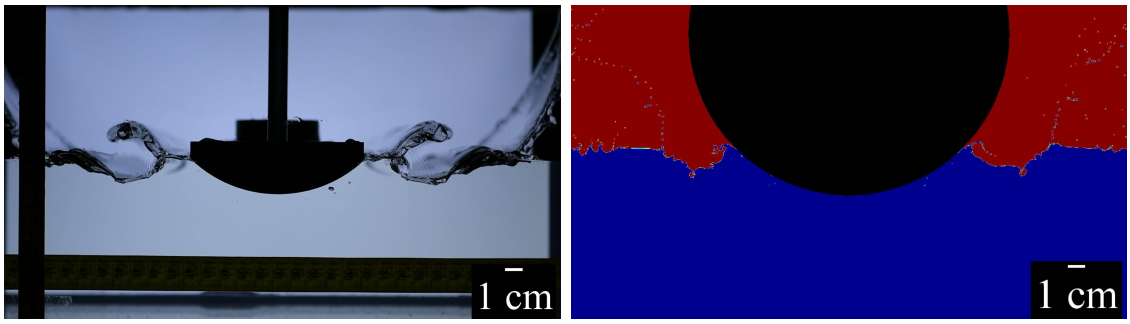

Figure 5.31: *Case E* at $t = 0.193[s]$, $t^* = 1.111[-]$

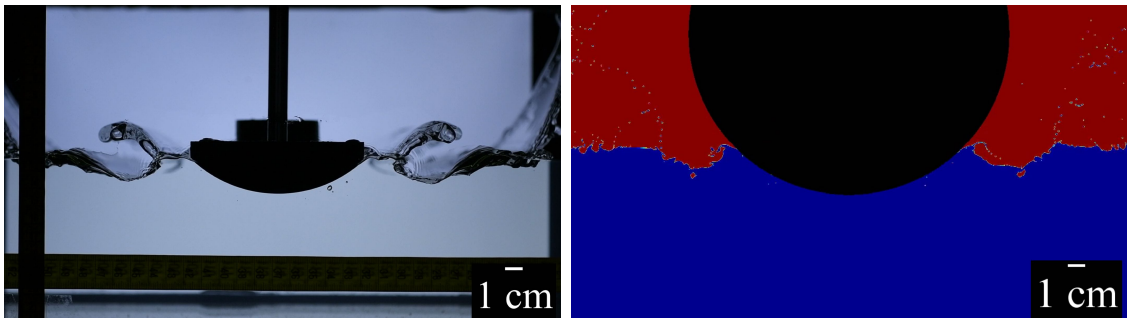

Figure 5.32: *Case E* at $t = 0.200[s]$, $t^* = 1.152[-]$

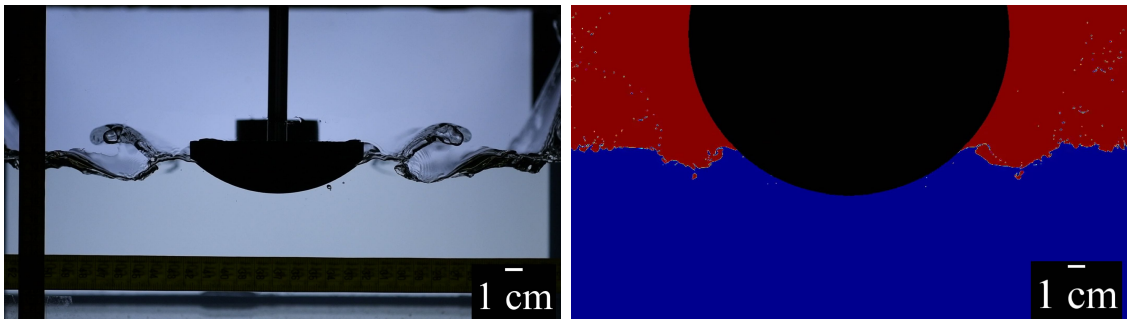

Figure 5.33: *Case E* at $t = 0.208[s]$, $t^* = 1.198[-]$

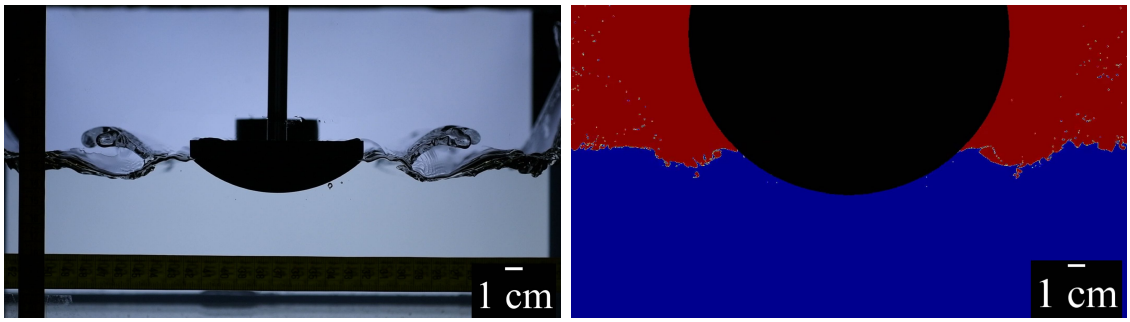

Figure 5.34: *Case E* at $t = 0.218[s]$, $t^* = 1.255[-]$

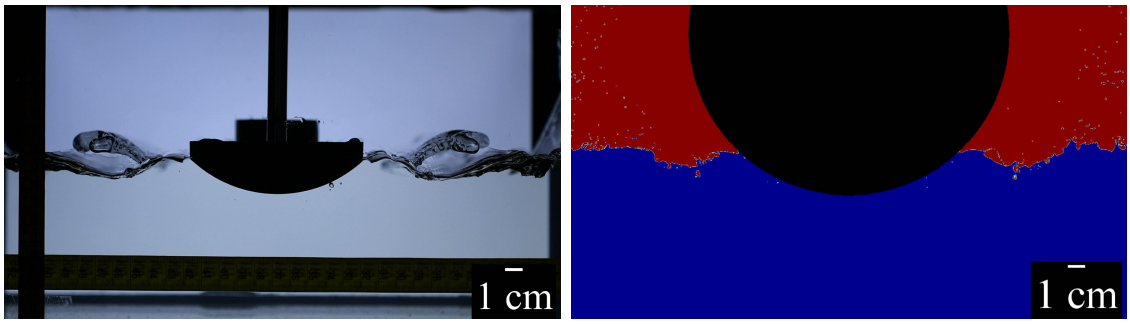

Figure 5.35: *Case E* at $t = 0.225[s]$, $t^* = 1.296[-]$

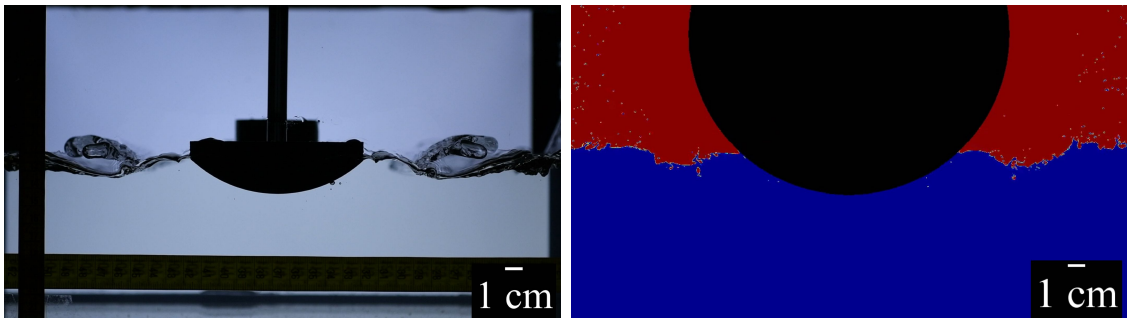

Figure 5.36: *Case E* at $t = 0.233[s]$, $t^* = 1.342[-]$

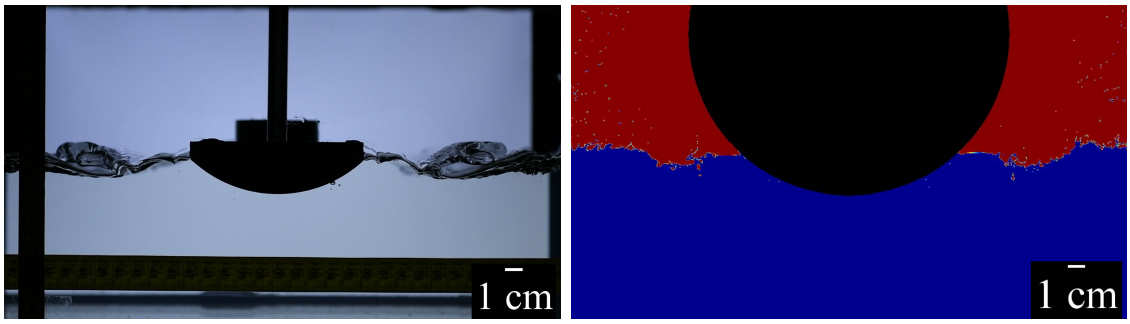

Figure 5.37: *Case E* at $t = 0.243[s]$, $t^* = 1.399[-]$

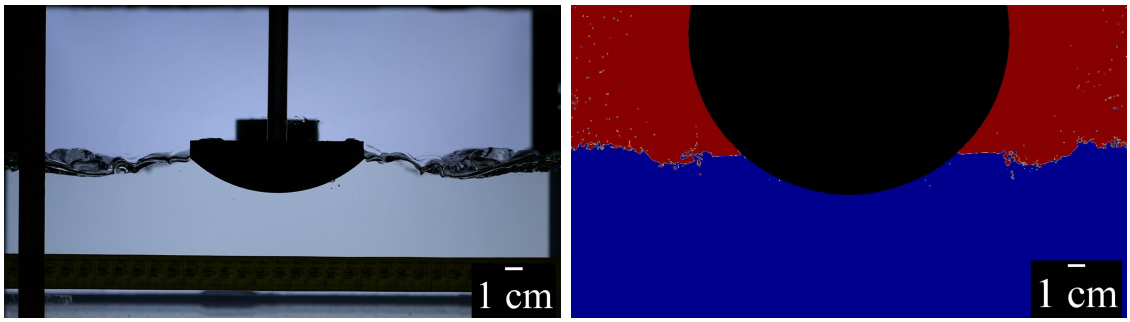

Figure 5.38: *Case E* at $t = 0.250[s]$, $t^* = 1.440[-]$

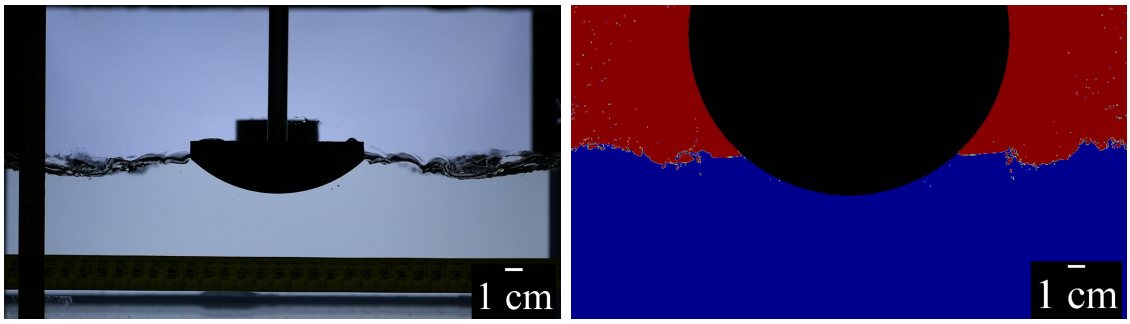

Figure 5.39: *Case E* at $t = 0.258[s]$, $t^* = 1.486[-]$

During this last investigated interval, from fig. 5.26 to fig. 5.39 it can be observed how the interfaces differ in the reproduction of exact local effects, but still, most of the main characteristics of the experimental case are replicated by the simulation.

Spilling in the main waves coming from the impact evolves similarly in both the experiment and the simulation.

Air gaps located at the back of the main waves (region of the waves closer to the solid), do not evolve as accurately in the simulation when compared to the experiment. This decrease in the water level in carried out faster in the experimental case for the same reason mentioned before. In the simulation, the solid remains still after the main impact, thus, the secondary wave structure is not reproduced as accurately as in the experiment.

This flow structure is coming not only from the reflection of the impact wave on the bottom, but also from the falling motion of the cylinder in the experiment. Therefore, this secondary wave does not carry as much momentum as in the experimental case to thrust the main one with the same intensity.

5.2.2 Interface comparison for *Case A*

The evolution of the experimental and simulated interfaces of *Case A* is presented in the following figures. However, fewer images are displayed for the sake of conciseness.

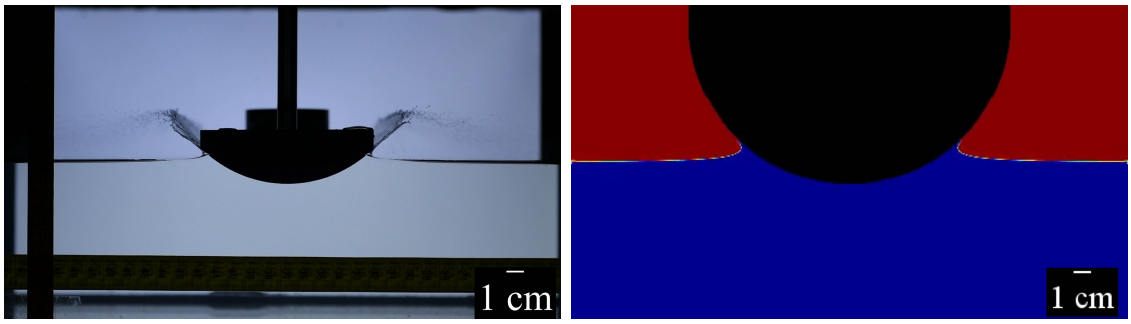

Figure 5.40: *Case A* at $t = 0.007[s]$, $t^* = 0.083[-]$

As in the previous case analyzed, the instant following the impact (fig. 5.40) presents some spilling due to the encounter of the water flow with the sharp edges of the experimental structure.

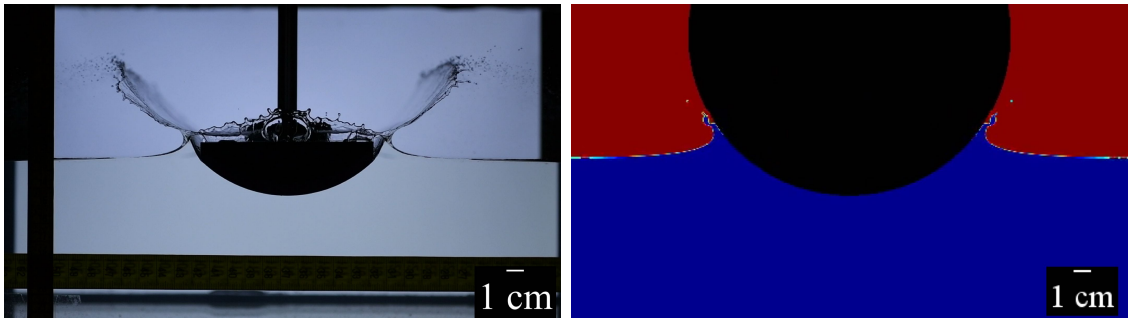

Figure 5.41: *Case A* at $t = 0.015[s]$, $t^* = 0.177[-]$

The minimum height instant following the impact is presented in fig. 5.41. At this moment, the two main waves generated from the impact begin their travel outwards. However, unlike the experimental case, the flow encounters a solid wall in the simulation. The reason why this is not observed in *Case E* is because it corresponds to a much smaller impact velocity, approximately half of the one attained in *Case A*. In the last case, the higher velocity generates a higher impact wave, which in turn impacts the solid itself, and, thus, breaks the main wave flow structure.

Figures 5.42 to 5.45 show several subsequent instants depicting the evolution of the interface.

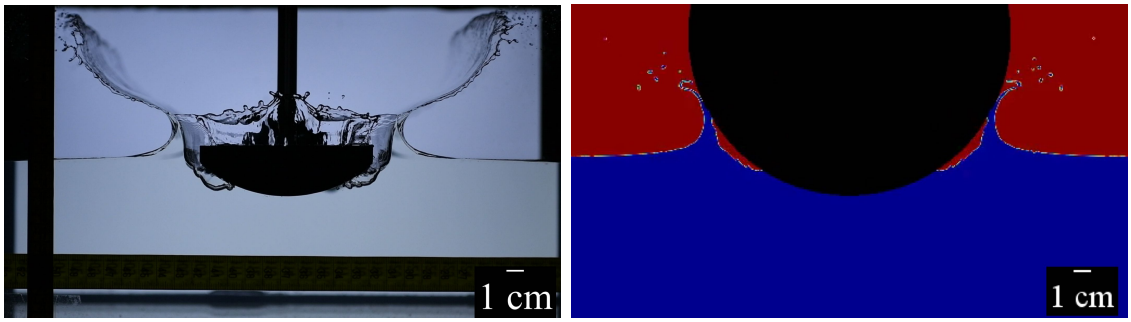

Figure 5.42: *Case A* at $t = 0.025[s]$, $t^* = 0.295[-]$

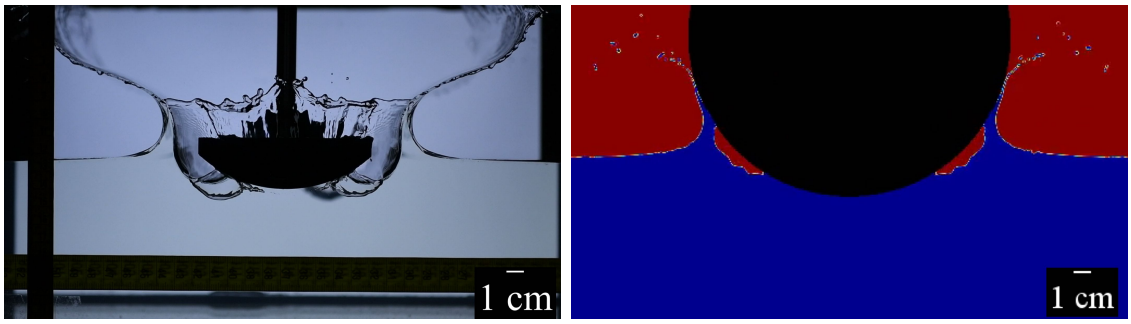

Figure 5.43: *Case A* at $t = 0.033[s]$, $t^* = 0.389[-]$

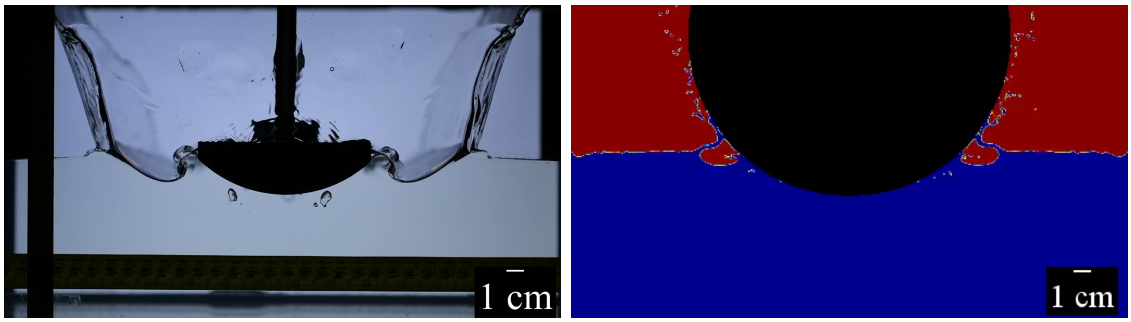

Figure 5.44: *Case A* at $t = 0.133[s]$, $t^* = 1.568[-]$

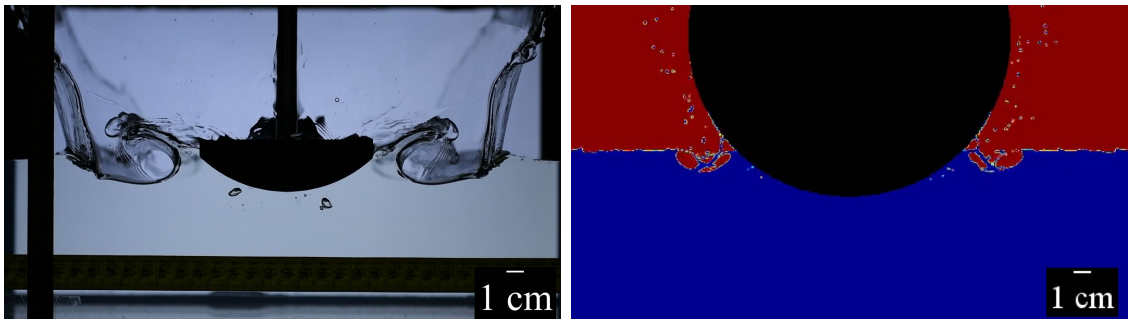

Figure 5.45: *Case A* at $t = 0.175[s]$, $t^* = 2.063[-]$

A similar low pressure region can be observed at the back of the initial main wave generated by the impact (fig. 5.42-fig. 5.43). In fig. 5.44, the secondary reflected wave structure is slightly appreciated in the simulation when compared to the experiment. In this case, not only the lack of motion of the cylinder, but also the water flow adhered to the solid (figures 5.42 and 5.43) that begun falling back down, were the two main factors for the high difference in size of this secondary wave. Finally, the air cavity generated by the main wave is transported outwards as time progresses (fig. 5.45).

After taking all of the above into consideration and comparing it with the results obtained for lower velocity cases (*Case E*, discussed in section 5.2.1), it is worth noting that improvements in the numerical code should be implemented in order to assure a correlation in the results of high speed cases (*Case A*).

6 Conclusions and future work

Several experiments were carried out and physical similarity was proved among them (section 5.1). It was found how the generated impact velocity could be considered constant in the vicinity of the impact instant. Although expected differences from the experiments arose due to the lack of oscillatory motion of the solid in the simulation, several of the main flow characteristics were reproduced with a significant degree of accuracy (section 5.2).

As mentioned in section 4.2.1, the implemented CFD code in *Basilisk* takes advantage of a simple approach to impose the boundary condition of the solid. Having compared both experiments and simulations, it is stated that the level of accuracy should not be considered high enough to assure with certainty that it can reproduce rigorously all the physical phenomena involved in this complex multiphase problem.

Despite this, it is observed how with such approach the similarity of the experimental and simulated flow is considerable. Therefore, this technique could serve as first contact with the problem, in which the potential of AMR coupled with the proposed numerical schemes (see section 4.2.2) stands out as a promising, powerful, and efficient numerical tool.

6.1 Future work

In this section, several ideas are proposed for future projects continuing the work presented in this one.

6.1.1 Improvements in the numerical section

First, it would be interesting to use the *embedded boundaries* technique to be able to compute forces, but most importantly, to ensure second-order accuracy. It is worth noting that this technique was not used in this project because it has not been extended outside the scope of 2D Stokes flows. S. Popinet, one of the authors of *Basilisk*, recently announced that they are interested in extending this technique to 3D and VOF flows. With this technique, the complete velocity time history of the experimental solid could be implemented in the code for a more accurate reproduction of the phenomena.

Moreover, surface tension could be implemented in the numerical code in order to provide an additional stabilizing mechanism to the flow apart from viscosity. However, this increases the computational time and, thus, a trade-off analysis between computational cost and accuracy of the results should be made.

On the contrary, removing droplets and bubbles could be interesting in order to reduce unnecessary computational time. A reference for this approach is provided in [40].

Finally, the mass of air would become increasingly important to the contribution of the problem in cases of high velocity models. Therefore, more attention should be placed on its effect on water entry.

6.1.2 Improvements in the experimental section

Although several improvements can be implemented for the numerical simulations, some minor upgrades can be applied to the experiments without increasing its cost significantly.

First, a lighter and buoyant structure could be used instead of a solid cylinder section. Also, the brass collar used as a stopping mechanism could be avoided in order to observe truthful oscillatory motion coming solely from the interaction between the structure and the water.

Additionally, two supplementary guiding shafts could be placed perpendicularly to the plane formed by the two existing ones. With this, the vertical motion of the solid could be compared to the results presented in this project.

7 Socio-economic framework

7.1 Financial analysis

The financial plan for the project is presented in this section. Several tools and resources were used in the development of this Bachelor's thesis.

Starting from the experimental setup, a list of materials used as well as their associated cost is presented in table 6.

Test materials	**Cost [€]**
PVC parts (estimated)	35
Stainless steel shaft	50.49
Sintered bronze bushings	10.3
Brass collar (estimated)	5

Table 6: Cost of materials used in tests

Estimated costs refer to parts that were not purchased, but were already in possession of the Fluid Mechanics Research Group at UC3M.

In table 7, the complete financial statement of the project is broken down.

Elements		**Cost [€]**
Materials		
	Test parts	100.79
Machining		
	CNC and operator's salary (estimated)	200
Equipment		
	DSLR camera Nikon D850	3110
	Tripod	200
	White light background screen	1000
	PC wattage consumption (estimated)	30
Licences		
	Free Software: Basilsik, GfsView, ImageJ	0
	Solid edge Student Version	0
	MATLAB Student R2019a	0 (56*)
Salary		
	Salary (estimated from [44])	3060
TOTAL		**7700.79**

Table 7: Complete financial statement of the project

Full access to MATLAB Student version R2019a is provided by UC3M. If this were not the case, the cost of the base licence with the packages used would be 56€. Estimated costs are due to the lack of precise figures. The salary was estimated with the number of ECTS required for the project.

7.2 Socio-economic impact

Aircraft design has a crucial impact on the socio-economic framework. Decisions during design phase affect the rest of the stages, thus influencing costs (manufacturing, repairs, etc.) and social implications (accidents).

SMAES (Smart Aircraft in Emergency Situations) was a project requested by EASA and 66.7% funded by the European Commission, that lasted from February 1, 2011 to October 31, 2014. As mentioned in [43], the desired outcome of the SMAES project was to "advance methodologies and simulation tools to support aircraft development from pre-project phase to certification". With this, the project aimed to enhance innovation in aircraft design compliant with the safety requirements. The overall budget was 5,732,492.60 €, and it was distributed among universities, research laboratories and industrial partners from the European Union.

An extensive experimental campaign served to support the work withing this field and to provide a reliable source for future analyses. Moreover, semi-analytical and numerical models were also developed and validated with the experimental results. Efforts were channeled towards more accurate and realistic CFD models, and to a proper fluid-structure integration. At the end, the main achievements were the extensive database generated, the improvement in models to predict satisfactorily the global behaviour of an aircraft ditching, and the significant advancement in the prediction of local phenomena (mainly involving pressure distributions).

SARAH (Increased Safety and robust certification for ditching of aircrafts and helicopters) is a similar project that will last from October 1, 2016 to September 30, 2019. Its main objectives are to improve aircraft and helicopter certification tools, derive a robust way to design new configurations prioritizing safety and use the methods obtained to supporting the pilot in water-landing scenarios. This project is part of the European Union Horizon 2020 research and innovation program, and counts with a total budget of approximately 6.6M€.

It can be seen how the applications proposed in this project are a current concern in the air transport industry. Several projects aim to improve the knowledge on this specific field, where several physical phenomenons occurs simultaneously. As mentioned in [43], "a planned or unplanned water-landing event occurs grossly speaking every 5 years". It is in the interest of the current society to advance in the generation of robust and reliable design methodologies that can improve the safety in an industry sector where a significant portion of transfers occur over water.

8 Regulatory framework

Certification Specifications for large aeroplanes, small and large rotorcrafts, CS-25,CS-27, and CS-29, respectively, were examined in order to comprehend the airworthiness requirements needed to certificate certain airborne vehicles in the event of an emergency landing condition. A general outline of these requirements surrounding ditching events can be seen in table 8.

CS.25.561	General (EMERGENCY LANDING CONDITIONS)
CS 25.563	Structural ditching provisions
CS 25.801	Ditching (EMERGENCY PROVISIONS)
CS 25.1411	General (SAFETY EQUIPMENT)
CS 25.1415	Ditching equipment

Table 8: Certification Specifications related to ditching for large aeroplanes

Identical sections exist for CS-27 and CS-29.

Essentially, these certifications agree in a similar prerequisite concerning ditching events, minimizing the probability of causing immediate injury to the passengers and ensuring the possibility of escape.

- "*minimize the probability that in an emergency landing on water, the behaviour of the aeroplane would cause immediate injury to the occupants or would make it impossible for them to escape.*" (CS-25.801(b))
- "*minimize the probability that when ditching, the behaviour of the rotorcraft would cause immediate injury to the occupants or would make it impossible for them to escape.*" (CS-27.801(b) and CS-29.801(b))

Finally, the AMC section of each CS manual, mentions that experiments using subscale models are an accepted mean of compliance of aircraft performance involved in a planned ditching maneuver.

References

[1] S. Popinet, F. De Vita, J. M. Fullana, G. Kirstetter, P. Y. Lagrée, E. Lane, J. L. Herrera and J. MacFarlane. “Basilisk website”. Basilisk-Basilisk. http://basilisk.fr/. (Accessed May 1, 2019)

[2] S. Popinet. “Gerris website”. Gerris Flow Solver. http://gfs.sourceforge.net/wiki/index.php/Main_Page. (Accessed May 1, 2019)

[3] ”Ditching of US Airways Flight 1549 (January 15, 2009)”. Wikipedia. https://en.wikipedia.org/wiki/US_Airways_Flight_1549. (Accessed June 5, 2019)

[4] U.S. Fish and Wildlife Service. ”Light float plane aircraft making a landing”. Wikipedia. https://commons.wikimedia.org/wiki/File:Light_float_plane_aircraft_making_a_landing.jpg. (Accessed June 5, 2019)

[5] C. W. Karl. ”Icon A5 landing”. Flickr. https://www.flickr.com/photos/cwkarl/37967175896. (Accessed June 5, 2019)

[6] ”Apollo 9 Splashdown”. NASA. https://www.nasa.gov/image-feature/apollo-9-splashdown. (Accessed June 5, 2019)

[7] G. S. Baker and E. M. Keary, ”Experiments with Full-Sized Machines (2d series)”, *British A.R.C. Reports and Memoranda No. 683*, 1920.

[8] Wm. Froude, ”P.5 Flying Boat N.86, Impact Tests. Experiments with Full-Sized Machines (3d series)”, *British A.R.C. Reports and Memoranda No. 926*, 1924.

[9] T. Von Kármán, ”The impact on seaplane floats during landing”, *NACA TN 321*, 1929.

[10] W. L. Mayo, ”Theoretical and experimental dynamic loads for a prismatic float having an angle of dead rise of 22-1/2°”, *NACA WR L5F15*, 1945.

[11] W. L. Mayo, ” Analysis and modifications of theory for impact of seaplanes on water”, *NACA TR 810*, 1945.

[12] H. A. Wagner, ”Planning of watercraft”, *NACA TM 1139*, 1948.

[13] W. L. Mayo, ”Hydrodynamic impact of a system with a single elastic mode I. Theory and generalized solution with an application to an elastic airframe”, *NACA TR 1074*, 1952.

[14] R. W. Miller and K. F. Merten, ”Hydrodynamic impact of a system with a single elastic mode II. Comparison of experimental force and response with theory”, *NACA TR 1075*, 1952.

[15] E. E. McBride and L. J. Fisher, ”Experimental investigation of the effect of rear-fuselage shape on ditching behaviour”, *NACA TN 2929*, 1953.

[16] S. Popinet, "Gerris: a tree-based adaptive solver for the incompressible Euler equations in complex geometries", *Journal of Computational Physics*, vol. 190, no. 2, pp. 572–600, 2003.

[17] A. Korobkin, "Analytical models of water impact", *European Journal of Applied Mathematics*, vol. 15, no. 6, pp. 821–838, 2004.

[18] H. Climent, L. Benitez, F. Rosich, F. Rueda and N. Pentecote, "Aircraft Ditching Numerical Simulation", presented at 25th Congress of International Council of the Aeronautical Sciences ICAS 2006. Hamburg, Germany, 3-8 September 2006.

[19] A. Iafrati and A. Korobkin, "Asymptotic estimates of hydrodynamic loads in the early stage of water entry of a circular disk", *Journal of Engineering Mathematics*, vol. 69, no. 2, pp. 199–224, 2011.

[20] D. J. Piro and K. J. Maki, "Hydroelastic wedge entry and exit", presented at 11th International Conference on Fast Sea Transport. Honolulu, Hawaii, USA, 2011.

[21] Y. M. Scolan and A. A. Korobkin, "Mixed boundary value problem in Potential Theory: Application to the hydrodynamic impact (Wagner) problem", *Comptes rendus - Mécanique*, vol. 340, no. 10, pp. 702–705, 2012.

[22] G. Baodong, L. Peiqing, Q. Qiulin, W. Jiawen, "Effect of pitch angle on initial stage of a transport airplane ditching", *Chinese Journal of Aeronautics*, vol. 26, no. 1, pp. 17–26, 2013.

[23] A. A. Korobkin, "A linearized model of water exit", *Journal of Fluid Mechanics*, vol. 737, pp. 368–386, 2013.

[24] A. A. Korobkin, T. Khabakhpasheva, S. Malenica, and Y. Kim, "A comparison study of water impact and water exit models", *International Journal of Naval Architecture and Ocean Engineering*, vol. 6, no. 4, pp. 1182–1196, 2014.

[25] S. Popinet, "A quadtree-adaptive multigrid solver for the Serre–Green–Naghdi equations", *Journal of Computational Physics*, vol. 302, no. C, pp. 336–358, 2015.

[26] H. Climent, G. Pastor and J. T. Viana, "Experimental Ditching Loads On Aeronautical Flexible Structures", presented at International Forum on Aeroelasticity and Structural Dynamics IFASD, Como - Italy, 25-28 June 2017.

[27] C. Bisagni and M. S. Pigazzini, "Modelling strategies for numerical simulation of aircraft ditching", *International Journal of Crashworthiness*, vol. 23, no. 4, pp. 377-394, 2018.

[28] M. Müller, M. Woidt, M. Haupt, and P. Horst, "Challenges of fully-coupled high-fidelity ditching simulations", *MATEC Web of Conferences*, vol. 233, 2018.

[29] P. Vega-Martínez, J. Rodríguez-Rodríguez, A. A. Korobkin and T. Khabakhpasheva, "Hydroelastic effects during the fast lifting of a disc from a water surface", *Journal Of Fluid Mechanics*, vol. 869, pp. 726–751, 2019.

[30] S. Popinet et al. "Basilisk C". Basilisk-Basilisk. http://basilisk.fr/Basilisk%20C. (Accessed June 15, 2019)

[31] S. Popinet et al. "Solvers and functions". Basilisk-Basilisk. http://basilisk.fr/src/README. (Accessed June 15, 2019)

[32] S. Popinet et al. "Navier-Stokes centered solver". Basilisk-Basilisk. http://basilisk.fr/src/navier-stokes/centered.h. (Accessed June 15, 2019)

[33] S. Popinet et al. "Bell-Collela-Glaz advection scheme". Basilisk-Basilisk. http://basilisk.fr/src/bcg.h. (Accessed June 15, 2019)

[34] S. Popinet et al. "Two-phase interfacial flows". Basilisk-Basilisk. http://basilisk.fr/src/two-phase.h. (Accessed June 15, 2019)

[35] S. Popinet et al. "Momentum-conserving advection of velocity". Basilisk-Basilisk. http://basilisk.fr/src/navier-stokes/conserving.h. (Accessed June 15, 2019)

[36] S. Popinet et al. "Reduced gravity". Basilisk-Basilisk. http://basilisk.fr/src/reduced.h. (Accessed June 15, 2019)

[37] S. Popinet et al. "Distance field computation from a 3D model". Basilisk-Basilisk. http://basilisk.fr/src/examples/distance.c. (Accessed June 15, 2019)

[38] S. Popinet et al. "Two-phase flow around RV Tangaroa". Basilisk-Basilisk. http://basilisk.fr/src/examples/tangaroa.c. (Accessed June 15, 2019)

[39] S. Popinet et al. "An example of moving solid". Basilisk-Basilisk. http://basilisk.fr/sandbox/popinet/movingcylinder.c. (Accessed June 15, 2019)

[40] "Droplets and bubbles removal library". Basilisk-Basilisk. http://basilisk.fr/sandbox/aberny/bubble/drop_stat.h. (Accessed June 15, 2019)

[41] "Initial Airworthiness, Certification Specifications (CSs)". European Union Aviation Safety Agency (EASA). https://www.easa.europa.eu/document-library/certification-specifications/reg/initial-airworthiness. (Accessed June 15, 2019)

[42] “Smart Aircraft in Emergency Situations”. European Commission. http://sarah-project.eu/. (Accessed June 15, 2019)

[43] “Increased Safety and robust certification for ditching of aircrafts and helicopters”. European Commission. https://cordis.europa.eu/project/rcn/97150/factsheet/en. (Accessed June 15, 2019)

[44] “Average Entry-Level Aerospace Engineer Salary”. Payscale website. https://www.payscale.com/research/ES/Job=Aerospace_Engineer/Salary/da0d197e/Entry-Level. (Accessed June 15, 2019)